

## **A pH-dependent microkinetic modeling guided synthesis of porous dual-atom catalysts for efficient oxygen reduction in Zn-air batteries**

Tingting Li<sup>a,†</sup>, Di Zhang<sup>b,†</sup>, Yun Zhang<sup>a</sup>, Danli Yang<sup>a</sup>, Runxin Li<sup>c</sup>, Fuyun Yu<sup>d</sup>, Kengqiang Zhong<sup>d</sup>, Xiaozhi Su<sup>e</sup>, Tianwei Song<sup>f</sup>, Long Jiao<sup>f</sup>, Hai-Long Jiang<sup>f</sup>, Guo-Ping Sheng<sup>d</sup>, Jie Xu<sup>c\*</sup>, Hao Li<sup>b\*</sup>, Zhen-Yu Wu<sup>a\*</sup>

<sup>a</sup>Department of Chemistry, Institute of Innovative Material, Guangdong Provincial Key Laboratory of Sustainable Biomimetic Materials and Green Energy, Southern University of Science and Technology, Shenzhen 518055, China

<sup>b</sup>Advanced Institute for Materials Research (WPI-AIMR), Tohoku University, Sendai, 980-8577, Japan

<sup>c</sup>College of Chemistry and Materials Engineering, Wenzhou University, Wenzhou, Zhejiang 325035, China

<sup>d</sup>CAS Key Laboratory of Urban Pollutant Conversion, Department of Environmental Science and Engineering, University of Science and Technology of China, Hefei 230026, China

<sup>e</sup>Shanghai Synchrotron Radiation Facility, Shanghai Advanced Research Institute, Chinese Academy of Sciences, Shanghai 201210, China

<sup>f</sup>Hefei National Research Center for Physical Sciences at the Microscale, Department of Chemistry, University of Science and Technology of China, Hefei 230026, China

\*E-mail: wuzy@sustech.edu.cn; li.hao.b8@tohoku.ac.jp; jiexu@wzu.edu.cn

†These authors contributed equally to this work.

## Experimental Section

**Computational method.** DFT calculations were used to determine the binding energies of ORR adsorbates. The generalized gradient approximation method with the revised Perdew-Burke-Ernzerhof functional (RPBE)<sup>1,2</sup> was employed to describe electronic exchange and correlations. The core electrons were described using a projector augmented-wave method<sup>3</sup>, while the valence electrons were described by expanding the Kohn-Sham wavefunctions in a plane-wave basis set<sup>4</sup> with a cutoff of at least 520 eV. The Monkhorst-Pack grid was used to sample the Brillouin zone, satisfying the condition that the product of the number of k-points in any direction and the length of the basis vector in that direction,  $k \times a$ , should be greater than 15 Å. The structure files (CONTCAR-typed) of DACs are available at [https://github.com/tohokudizhang/M2-N-C\\_structures](https://github.com/tohokudizhang/M2-N-C_structures). Please refer to the Supplementary Information for complete computational and modeling details.

### 1. Binding Free Energy Calculations

The density functional theory (DFT) calculations were performed using the Vienna ab initio simulation package (VASP) to determine the binding energies of ORR adsorbates for scaling relations. The electronic exchange and correlations were described using the revised Perdew-Burke-Ernzerhof (RPBE) functional<sup>1,2</sup> with the generalized gradient approximation method. The valence electrons were described by the Kohn-Sham wave functions expanded in a plane-wave basis set<sup>4</sup>, with a cutoff of 520 eV. The method used to describe core electrons was a projector augmented-wave method<sup>3</sup>. We ensured convergence of electronic energy to  $10^{-5}$  eV and structural relaxation to 0.05 eV Å<sup>-1</sup>. To sample the Brillouin zone, we used a Monkhorst-Pack grid that satisfies the condition that the product of the number of k-points in any direction and the length of the basis vector in that direction,  $k \times a$ , should be greater than 15 Å. Spin-polarization was considered in all calculations. To guarantee adequate

spacing, we placed a vacuum spacing of at least 15 Å perpendicular to the surface. We used the Atomic Simulation Environment (ASE) package to manipulate the crystal structure and generate input<sup>5</sup>.

We calculated the electronic binding energies using the total energies of H<sub>2</sub> and H<sub>2</sub>O as the energy references, as shown in Equations \\* MERGEFORMAT (1)-\\* MERGEFORMAT (3):

$$E_{O^*} = E_{slab-O^*} - E_{slab} - E_{H_2O} + E_{H_2} \quad \backslash*$$

MERGEFORMAT (1)

$$E_{HO^*} = E_{slab-HO^*} - E_{slab} - E_{H_2O} + \frac{1}{2}E_{H_2} \quad \backslash*$$

MERGEFORMAT (2)

$$E_{HOO^*} = E_{slab-HOO^*} - E_{slab} - 2E_{H_2O} + \frac{3}{2}E_{H_2} \quad \backslash*$$

MERGEFORMAT (3)

Herein,  $E_{slab-ads^*}$  represents the total energy of the surface with the adsorbates,  $E_{slab}$  represents the total energy of a slab surface,  $E_{H_2O}$  is the total energy of an H<sub>2</sub>O molecule in vacuum, and  $E_{H_2}$  is the total energy of an H<sub>2</sub> molecule in vacuum.

The binding free energies of all adsorbates on M-N-C catalysts were calculated using the computational hydrogen electrode (CHE) method<sup>6</sup>, including the entropic, zero-point energy (ZPE), and solvation corrections, as shown in Equation \\* MERGEFORMAT (4). The results of these calculations are shown in **Table S1**<sup>Ref.7</sup>. For the adsorption free energies of H<sub>2</sub>O<sub>2</sub>, we used the scaling relationship derived from the previous study<sup>8</sup>.

$$G_{ads^*} = E_{ads^*} + \Delta ZPE - T\Delta S + E_{solv} \quad \backslash*$$

MERGEFORMAT (4)

## 2. Electric Fields and pH-Dependent Modelling

To describe the potential and pH dependence, we related the electric fields to both the standard

hydrogen electrode (SHE) and reversible hydrogen electrode (RHE) potential using a parallel-plate capacitor model. Equation \\* MERGEFORMAT (5) describes the model, where  $\sigma$  represents charge density,  $\epsilon_0$  refers to vacuum permittivity ( $8.85 \times 10^{-12}$  F m<sup>-1</sup>),  $\epsilon$  refers to dielectric constant (unitless),  $C_H$  represents Helmholtz capacitance ( $\mu\text{F cm}^{-2}$ ),  $U_{SHE}$  represents potential vs. SHE, and  $U_{PZC}$  represents potential at the point of zero charges (PZCs) vs. SHE.

$$\frac{\sigma}{\epsilon\epsilon_0} = \frac{C_H (U_{SHE} - U_{PZC})}{\epsilon\epsilon_0} \quad \backslash^*$$

MERGEFORMAT (5)

Fumagalli et al<sup>9</sup>. demonstrated that the dielectric constant of water near a surface is 2. The Helmholtz capacitance ( $C_H$ ) can vary with the surface and potential, but typically ranges between 20 and 30 over the majority of the potential range, with higher values near the point of zero charge (PZC). For simplicity, we assumed a constant  $C_H$  of 25  $\mu\text{F cm}^{-2}$  across all surfaces<sup>10</sup>.

To measure the response of an adsorbate to the field, we fitted a second-order polynomial to the calculations for each adsorbate over the range of fields. We then used Equation \\* MERGEFORMAT (6) to determine the intrinsic dipole moment ( $\mu$ ) and polarizability ( $\alpha$ ) values.

$$G_{ads} = G_{ads}^{PZC} + \mu E - \frac{\alpha}{2} E^2 \quad \backslash^*$$

MERGEFORMAT (6)

Herein,  $G_{ads}^{PZC}$  refers to the binding energy of adsorbate at the PZC, which corresponds to the energy calculated with no applied field. These fits, along with values for  $\mu$  and  $\alpha$  for each adsorbate on each electrode, are from our previous work<sup>11</sup>.

The CHE was used to correct the binding energies for RHE dependence using Equation \\* MERGEFORMAT (7), where  $n$  refers to the number of electrons (relative to water),  $e$  refers to the charge of an electron, and  $U_{RHE}$  refers to the potential versus RHE.

$$G_{ads} = G_{ads,U_{RHE}=0} - neU_{RHE} \quad \backslash*$$

MERGEFORMAT (7)

Ultimately, the free energy of adsorbate at the given  $U_{RHE}$  and  $U_{SHE}$  is shown by Equation \\*

MERGEFORMAT (8):

$$G_{ads} = G_{ads}^{PZC} + \mu \frac{C_H(U_{SHE} - U_{PZC})}{\epsilon\epsilon_0} - \frac{\alpha}{2} \left( \frac{C_H(U_{SHE} - U_{PZC})}{\epsilon\epsilon_0} \right)^2 - neU_{RHE} \quad \backslash*$$

MERGEFORMAT (8)

### 3. Determining the Potential of Zero Charge

In this study, we used implicit methods, VASPsol<sup>12,13</sup>, to determine the computational PZCs for DACs. We set the VASPsol parameters to default values, including a bulk dielectric constant  $\epsilon_k = 78.4$ , dielectric cavity width  $\sigma = 0.6$ , cutoff charge density  $\rho_{cut} = 0.0025 \text{ \AA}^{-3}$ , and a surface tension parameter of  $0.525 \text{ meV/\AA}^2$ . Trasatti et al.<sup>14</sup> showed that  $U_{PZC}$  can be directly derived from the work function of a material in ion-free water  $\phi$  using equation \\* MERGEFORMAT (9).

$$\phi = eU_{PZC} + \phi_{SHE} \quad \backslash*$$

MERGEFORMAT (9)

Here,  $\phi_{SHE}$  represents the absolute potential energy of the SHE. It is important to note that the value of  $\phi_{SHE}$  can vary depending on the experiment conducted (ranging from 4.3 to 4.8 eV). However, in this study, the recommended value of 4.44 eV by the International Union of Pure and Applied Chemistry (IUPAC) was used.

### 4. Microkinetic Modeling of ORR on M-N-C Catalysts

Microkinetic modeling of the ORR volcano was based on the approach outlined by Hansen et al.<sup>15</sup> and Kelly et al.<sup>10</sup> using the CatMAP package<sup>16</sup>. Rates for intermediate steps were calculated using equation (10):

$$rate = k_f \prod \theta_{react} - k_r \prod \theta_{prod} \quad (10)$$

where  $\theta_{react}$  and  $\theta_{prod}$  are the coverages of reactants and products, respectively. The rate constant  $k$  was calculated as the function of reaction prefactor  $A$  ( $s^{-1}$ ), activation free energy  $G_a$ , Boltzmann constant  $k_B$ , and reaction temperature  $T$ :

$$k = Ae^{-\frac{G_a}{k_B T}} \quad (11)$$

The intermediate reactions considered in the modeling are shown in Reactions (12)-(19):



Reaction (12) describes the diffusion of aqueous  $O_2$  through a Nernstian diffusion layer, which can be generally modeled as a chemical step with a rate of  $8 \times 10^5 s^{-1}$  (corresponding to a RDE rotation rate of 1600 rpm), as shown by Hansen et al.<sup>15</sup> In this study, to determine the kinetic turnover frequency (TOF), we utilized a hypothetical rate of  $1 \times 10^{10} s^{-1}$  for  $O_2$  diffusion. Reaction (13) represents the adsorption of  $O_2$  on the catalyst. A prefactor of  $1 \times 10^{10} s^{-1}$  was also used for this step<sup>15</sup>. Reactions (14)-(18) involve proton-electron transfer steps, where the energy of the proton-electron pair is represented by the energy of half of an  $H_2$  molecule according to the CHE method<sup>6</sup>. Reactions (14)-(18) describe the standard associative pathway for  $4e^-$  ORR, while reactions (17)-(18) represent the  $2e^-$  ORR process.

For Reaction (15), where the O-O bond is broken along with protonation, we used Equation (20) developed by Dickens et al.<sup>17</sup> to describe the activation energy of the O-O bond-breaking:

$$G_{TS} = 0.99G_{HOO^*} - 0.25 + 0.42U_{RHE} \quad (20)$$

For all other proton transfers, which did not include any other bond breaks, we used an intrinsic barrier of 0.26 eV and assumed the transfer coefficient was 0.5<sup>Ref.15</sup>. Prefactors for all of the proton-electron transfer steps were set as  $1 \times 10^9 \text{ s}^{-1}$  to account for solvent reorganization<sup>10</sup>. The energies of aqueous and double-layer O<sub>2</sub> were set to 5.19 eV at 0 V/RHE based on previous studies<sup>10,18</sup>, and the O<sub>2</sub> mole fraction was set to  $2.34 \times 10^{-5}$ , corresponding to 1 atm O<sub>2</sub> gas in equilibrium with water.

**Chemicals.** All chemicals were commercially available and used without further purification. Cobalt(II) chloride hexahydrate (CoCl<sub>2</sub>•6H<sub>2</sub>O), Iron(III) nitrate nonahydrate (Fe(NO<sub>3</sub>)<sub>3</sub>•9H<sub>2</sub>O), ammonium persulfate ((NH<sub>4</sub>)<sub>2</sub>S<sub>2</sub>O<sub>8</sub>), and *o*-Phenylenediamine (*o*PD) were purchased from Aldrich. Nafion solution (5 wt%) was purchased from Canrd Technology Co. Ltd. Silica (SiO<sub>2</sub>) powder (7 nm) was purchased from Sigma-Aldrich. Pt/C (20 wt%) was purchased from Shanghai Chuxi Industrial Co. Ltd. Millipore water (18.2 MΩ•cm) was used throughout all experiments.

**Synthesis of Fe<sub>1</sub>Co<sub>1</sub>-N-C catalyst.** Typically, 1.0 g *o*PD, 0.72 g Fe(NO<sub>3</sub>)<sub>3</sub>•9H<sub>2</sub>O, 0.40 g CoCl<sub>2</sub>•6H<sub>2</sub>O, and 1.0 g SiO<sub>2</sub> nanopowder (7 nm) were added into 50 mL 1.0 M HCl and then sonicated for 0.5 h and stirred for another 0.5 h. After that, 3.0 g (NH<sub>4</sub>)<sub>2</sub>S<sub>2</sub>O<sub>8</sub> was dissolved in 15 mL 1.0 M HCl and then added dropwise into the above solution with stirring in an ice bath and stirred for 24 h for polymerizing *o*PD. The mixture was dried by using a rotary evaporator. The obtained mixed powder was then subjected to pyrolysis at 700-1000 °C (800 °C as the optimized temperature) for 2 h under a flowing N<sub>2</sub> atmosphere (60 mL min<sup>-1</sup>). The SiO<sub>2</sub> templates were etched out by 2.0 M NaOH, and unstable metallic species were removed by 2.0 M H<sub>2</sub>SO<sub>4</sub> at 95 °C, respectively. Finally, the product

was activated by CO<sub>2</sub> (60 mL min<sup>-1</sup>) at 800 °C for 10-40 min (20 min as the optimized time) to form the Fe<sub>1</sub>Co<sub>1</sub>-N-C catalyst. The heating and cooling step was performed in a N<sub>2</sub> atmosphere for CO<sub>2</sub> activation process.

**Synthesis of reference Fe<sub>1</sub>-N-C, Co<sub>1</sub>-N-C, and N-C catalysts.** The synthesis processes for Fe<sub>1</sub>-N-C, Co<sub>1</sub>-N-C, and N-C catalysts were similar to that of Fe<sub>1</sub>Co<sub>1</sub>-N-C, with the only difference being that 1.44 g Fe(NO<sub>3</sub>)<sub>3</sub>•9H<sub>2</sub>O, 0.80 g CoCl<sub>2</sub>•6H<sub>2</sub>O and no metal salt were added for synthesizing Fe<sub>1</sub>-N-C, Co<sub>1</sub>-N-C and N-C, respectively.

**Characterization.** XRD data were collected on a Rigaku SmartLab 9KW Powder X-ray diffractometer using Cu K $\alpha$  radiation (40 kV, 40 mA) at room temperature. Inductively coupled plasma mass spectrometry (ICP-MS) measurements were carried out on an Agilent 8800 instrument. Raman spectra were collected on a LabRAM HR Evolution spectrometer system and excited by a 532 nm laser. Transmission electron microscope (TEM, JEM-2100Plus) was used to investigate morphologies of samples. The high-angular annular dark field scanning transmission electron microscopy (HAADF-STEM) and EDS elemental mapping were acquired by the FEI Titan Cubed Themis G2 300 with a probe corrector and a monochromator at 200 kV. X-ray photoelectron spectroscopy (XPS) spectra were obtained on a PHI 5000 VersaProbe III using Al K $\alpha$  radiation. The N<sub>2</sub> adsorption-desorption analysis was performed on a Micromeritics ASAP 2460 Version 3.01 analyzer at 77 K using Barrett-Emmet-Teller calculations for the surface area.

**XAS measurements and analysis.** XAS spectra at the Fe and Co K-edge were measured at the BL 14W1 beamline of the Shanghai Synchrotron Radiation Facility (SSRF), China, operated at 2.5 GeV with a maximum current of 250 mA. The data was collected in transmission/fluorescence mode using an ionization chamber by Si(111) double crystal monochromator. All spectra were collected in ambient

conditions. The EXAFS data were extracted and processed according to the standard procedures using the ATHENA module implemented in the IFEFFIT software packages. The  $k^3$ -weighted EXAFS spectra were obtained by subtracting the post-edge background from the overall absorption and then normalizing with respect to the edge-jump step. Subsequently,  $k^3$ -weighted  $\chi(k)$  data of Fe/Co K-edge were Fourier transformed to real ( $R$ ) space using a Hanning window ( $d_k = 1.0 \text{ \AA}^{-1}$ ) to separate the EXAFS contributions from different coordination shells. To obtain the quantitative structural parameters around central atoms, least-squares curve parameter fitting was performed using the ARTEMIS module of the IFEFFIT software packages.

**Electrochemical ORR measurements.** The ORR performance was investigated by using an electrochemical station (CHI760E) with a conventional three-electrode system. A Hg/HgCl<sub>2</sub> electrode (3.5 M KCl) and graphite rod were used as reference and counter electrode, respectively. For preparing a uniform catalyst ink, 5.0 mg catalyst was dispersed in 980  $\mu\text{L}$  isopropanol (IPA) and 20  $\mu\text{L}$  5% Nafion solution under sonication for at least 30 min. Then, a certain volume of the catalyst ink was dropped onto the polished glassy carbon rotating disk electrode (RDE, diameter is 5 mm, area is 0.196 cm<sup>2</sup>) or rotating ring disk electrode (RRDE, diameter is 5.61 mm, area is 0.2475 cm<sup>2</sup>), leading to a desirable catalyst loading. The mass loading was 0.6 mg<sub>total</sub> cm<sup>-2</sup> for M-N-C or N-C and 0.04 mg<sub>Pt</sub> cm<sup>-2</sup> for Pt/C. ORR performance was measured in O<sub>2</sub>-saturated 0.1 M KOH solution. All reported potentials in this work are referenced to the reversible hydrogen electrode (RHE) unless noted otherwise. The SCE was calibrated with a RHE potential by using the conversion equation  $E_{\text{vs. RHE}} = E_{\text{vs. SCE}} + 0.2415 + 0.059\text{pH}$ . Before measurements, the working electrode was subjected to 100 CV cycles in the potential range of 0-1.2 V vs. RHE at 100 mV s<sup>-1</sup> to reach a stable state. Linear sweep voltammetry (LSV) measurements were carried out on RDE with a sweep rate of 5 mV s<sup>-1</sup> at a rotation speed of

1600 rpm for the acquisition of polarization curves. The RRDE measurements were performed at a constant ring potential of 1.2 V vs. RHE. The onset potential was defined as the potential required for generating a current density of -0.1 mA cm<sup>-2</sup> in LSV curves. The electron transfer number was calculated by Koutecky-Levich (K-L) equation (21) and (22):

$$\frac{1}{J} = \frac{1}{J_K} + \frac{1}{J_L} = \frac{1}{J_K} + \frac{1}{B\omega^{1/2}} \quad (21)$$

$$B = 0.62nFC_0D_0^{2/3}\nu^{-1/6} \quad (22)$$

where  $J$  is the measured current density,  $J_K$  is the kinetic diffusion current density,  $J_L$  is the kinetic limiting current density,  $B$  is the reciprocal of the slope,  $\omega$  is the angular velocity ( $\omega = 2\pi N$ ,  $N$  is the rotation speed),  $n$  is transferred electron number,  $F$  is Faraday constant (96485 C mol<sup>-1</sup>),  $C_0$  is the saturated concentration of O<sub>2</sub> (1.2×10<sup>-6</sup> mol cm<sup>-3</sup>),  $D_0$  is the diffusion coefficient of O<sub>2</sub> (1.9×10<sup>-5</sup> cm<sup>2</sup> s<sup>-1</sup>), and  $\nu$  is the kinetic viscosity (0.01 cm<sup>2</sup> s<sup>-1</sup>).

RRDE measurements were used to investigate the ORR selectivity of the catalysts. The H<sub>2</sub>O<sub>2</sub> yield ( $H_2O_2\%$ ) and electron transfer number ( $n$ ) were calculated from the following equations (23) and (24):

$$H_2O_2\% = 200 \times \frac{I_{R/N}}{(I_{R/N}) + I_D} \quad (23)$$

$$n = 4 \times \frac{I_D}{(I_{R/N}) + I_D} \quad (24)$$

where  $I_R$  and  $I_D$  are the ring and disk currents, respectively, and  $N$ , which is 0.37, is the current collection efficiency of the Pt ring. All the measured potentials were 100% IR-compensated unless otherwise specified.

The electrochemically active surface area (ECSA) was achieved by using a CV scan method within a non-Faradaic potential range of 0.21-0.31 V versus RHE at the scan rates from 2 to 10 mV s<sup>-1</sup>.  $C_{dl}$  was estimated by plotting the  $\Delta J$  ( $\Delta J = (J_{anodic} - J_{cathodic})/2$ ) at 0.26 V versus RHE against scan rate, and

the linear slope was equivalent to the  $C_{dl}$ . The ECSA was defined as the electrochemically active area of an electrode with 1 cm<sup>2</sup> of geometric area. And the ECSA was calculated by the equation (25) as follow:

$$\text{ECSA} = \frac{C_{dl}}{C_s} A \quad (25)$$

where the  $C_s$  is the specific capacitance of flat electrode, A is the geometric area of the electrode (0.19625 cm<sup>2</sup>). We assumed that the  $C_s$  are the same for the Fe<sub>1</sub>Co<sub>1</sub>-N-C, Fe<sub>1</sub>-N-C, Co<sub>1</sub>-N-C, and N-C and took the value of 0.02 mF cm<sup>-2</sup> as suggested for the carbon materials based on a previous work<sup>19</sup>. All of the current densities reported in this work are based on geometric surface area unless otherwise specified.

**In-situ ATR-SEIRAS spectroscopic characterization**<sup>20</sup>. Typically, the preparation method of catalyst ink is the same as that used in electrochemical measurements. A polycrystalline gold film deposited via ion sputtering on the reflecting plane of a silicon prism was utilized as the working electrode and the catalyst was placed on it. An Ag/AgCl electrode and a graphite rod were used as the reference electrode and counter electrode, respectively. All spectroscopic measurements were collected with 4 cm<sup>-1</sup> resolution and at least 128 coadded scans using a Thermo Fisher iS50 Fourier-transform infrared reflection spectrometer equipped with a liquid nitrogen-cooled MCT detector. The configuration of the spectro-electrochemical cell is shown in **Fig. 5a**. Electrochemical measurements were conducted using a CHI760E electrochemical workstation and measured in an O<sub>2</sub>-saturated 0.1 M KOH solution.

**In-situ Raman spectroscopic tests.** In-situ Raman spectra were recorded with a LabRAM HR Evolution Raman microscope using a 532 nm line of an Ar-ion laser, and the microscope objective lens was ×50 magnification. Before the experiment, the Raman frequency was calibrated using a Si

wafer ( $520.6 \text{ cm}^{-2}$ ). The in-situ spectro-electrochemical cell was also carried out with a three-electrode configuration. During the ORR process, the cell was controlled by an electrochemical workstation (CHI760E) for the *i-t* tests from 1.0 to 0.1 V vs. RHE. Each potential was held for 10 min, while the Raman spectra were collected simultaneously for 8 min with 20 accumulations to enhance its signal-to-noise ratio.

**Zn-air battery tests.** Zn-air battery tests were performed in an aqueous solution of 6.0 M KOH and 0.2 M Zn(Ac)<sub>2</sub> at room temperature. A sandwich-like structure was used for air cathode, which is composed of a catalyst layer, a water-proof breathable membrane, and a Ni foam (current collector). The catalyst layer was prepared as follows. The carbon-based ORR catalyst (40 mg) was first added in ethanol (EtOH, 1 mL). Then the polytetrafluoroethylene (PTFE) emulsion (60 wt.%, 30  $\mu\text{L}$ ) was added into the above mixture. After mixing for 30 min and drying at room temperature to remove excessive EtOH, it was rolled out into a catalyst film by using a glass rod (diameter = 1 mm). Then, the catalyst film was cut into 8 pieces (1.0 cm  $\times$  1.0 cm). The catalyst loading is 5  $\text{mg}_{\text{cat}} \text{ cm}^{-2}$ . Finally, the catalyst film, water-proof breathable membrane, and Ni foam were compressed by tablet press at 10 MPa for 30 s to obtain the air cathode<sup>21</sup>. The air cathode should be stored in a vacuum environment before use. A polished Zn plate (purity 99.9 wt%, thickness 2.0 mm) was used as the anode. For comparison, the ZAB based on Pt/C as air cathode catalyst was also constructed. The power density profiles were generated by plotting power density against applied current density, which were performed by LSV technique at 10  $\text{mV s}^{-1}$  with CHI 760E electrochemical workstation. Power density was calculated by multiplying the applied current density by the corresponding battery voltage recorded during the galvanodynamic discharge experiments.

**Specific capacity:** Specific capacity refers to the amount of electric charge a material or device can

store or deliver per unit mass or volume, typically expressed in units of mAh g<sup>-1</sup> or Ah kg<sup>-1</sup>. Zinc-air batteries were fully discharged at a fixed current density (10, 20, 50, and 100 mA cm<sup>-2</sup>) until a failure of the battery life to explore the battery discharge specific capacity. The specific capacity (mAh g<sup>-1</sup>) based on the weight of consumed Zn are calculated according to Eqs. 1:

$$\text{Specific capacity} = \frac{\text{Discharge current} \times \text{Service hours}}{\text{the weight of consumed Zn}} \quad (26)$$

The specific capacities are 836.5, 794.2, 750.1, and 436.4 mAh g<sub>Zn</sub><sup>-1</sup>, respectively.

Energy density: Energy density refers to the amount of energy stored or delivered per unit of mass. It is commonly used to describe the efficiency of energy storage systems, such as batteries. Energy density is typically expressed in units Wh kg<sup>-1</sup>.

The energy density (Wh kg<sup>-1</sup>) based on the weight of consumed Zn are calculated according to Eqs. 2:

$$\text{Energy density} = \frac{\text{Discharge current} \times \text{Service hours} \times \text{Average discharge voltage}}{\text{the weight of consumed Zn}} \quad (27)$$

When the current densities are 10, 20, 50, and 100 mA cm<sup>-2</sup>, the energy densities are 1079, 794.2, 750.1, and 436.4 Wh g<sub>Zn</sub><sup>-1</sup>, respectively.

The open-circuit voltage of ZAB was tested by an electrochemical workstation (CHI760E). Furthermore, ZAB was fully discharged at a fixed current density (10, 20, 50, and 100 mA cm<sup>-2</sup>) until a failure of the battery life to explore the battery discharge specific capacity. ZAB discharge experiments at various current densities of 2, 5, 10, 20, 50, 100, 300, 500, and 600 mA cm<sup>-2</sup> were carried out for 90 min and 11 cycles to investigate rate capability of the catalyst-involved cathode. The long-term stability of ZABs was tested by the Neware battery test system (Shenzhen Neware, China,

10 min discharge, 5 min rest, and 10 min charge, with the current density of  $5 \text{ mA cm}^{-2}$ , capacity is 0.8 mAh), and the air cathode was based on  $\text{Fe}_1\text{Co}_1\text{-N-C} + \text{RuO}_2$  or  $\text{Pt/C} + \text{RuO}_2$  (mass ratio: 1:1). Zinc anodes were termly replaced with fresh ones. The catalyst layer preparation method is the same to the above process.

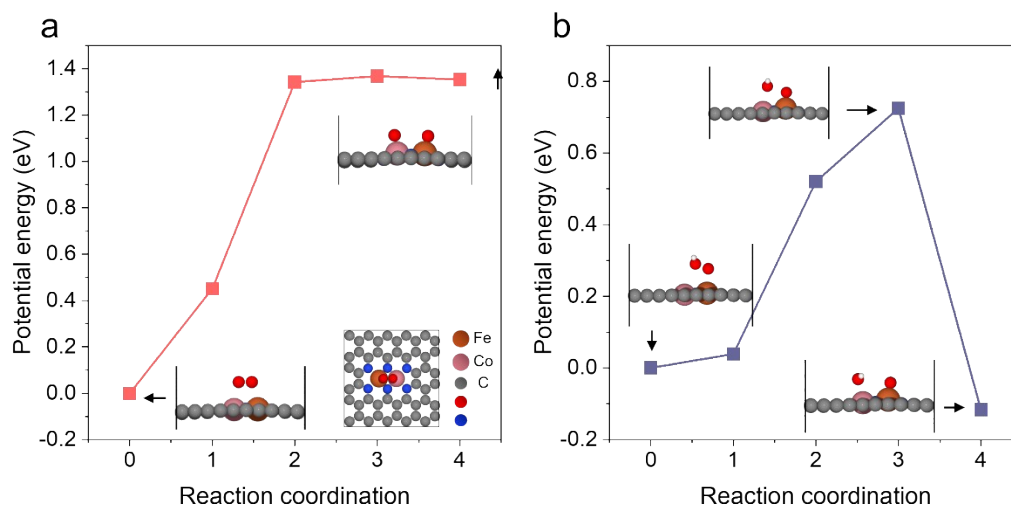


**Figure S1.** Reaction pathway energy for the direct O-O bond cleavage of O<sub>2</sub> and HOO on the Fe<sub>1</sub>Co<sub>1</sub>-N-C surface.

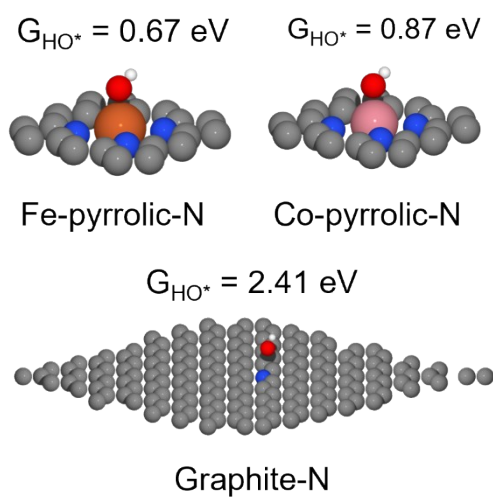


**Figure S2.** ORR activity analysis of Fe-pyrrolic-N, Co-pyrrolic-N, and graphite-N: Structural diagram and adsorption free energy of HO\*.

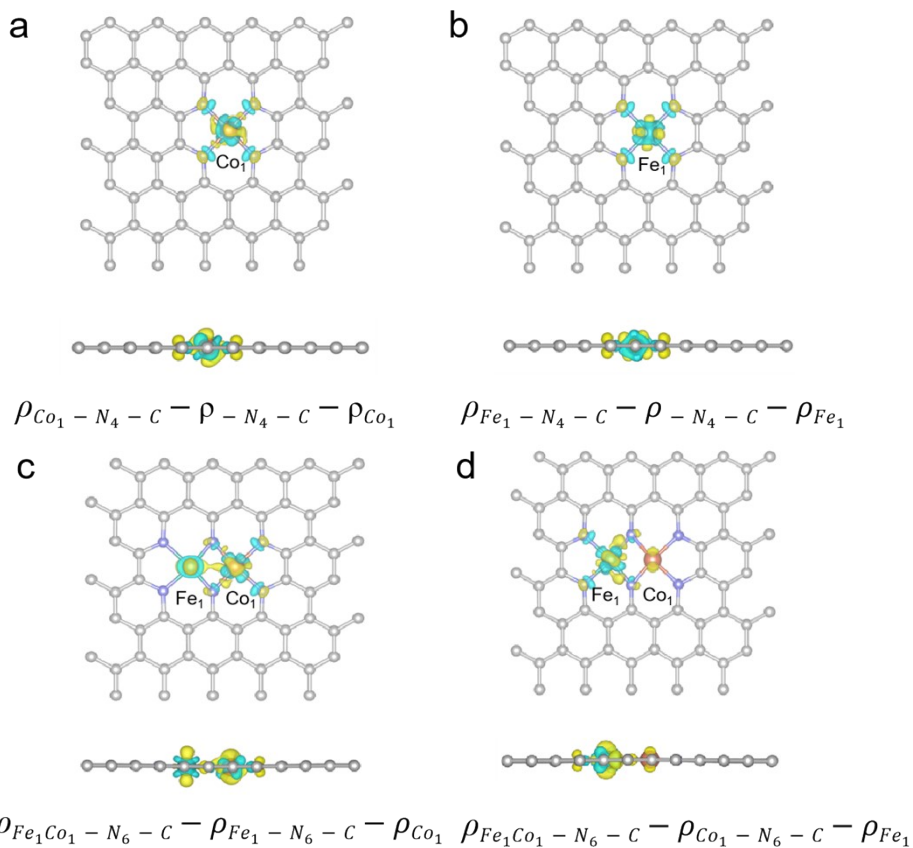


**Figure S3.** (a-d) Differential charge density analysis of DACs and SACs. In contrast to SACs, the metal atoms in DACs interact not only with the surrounding coordinated N atoms, but also with the other metallic atom.

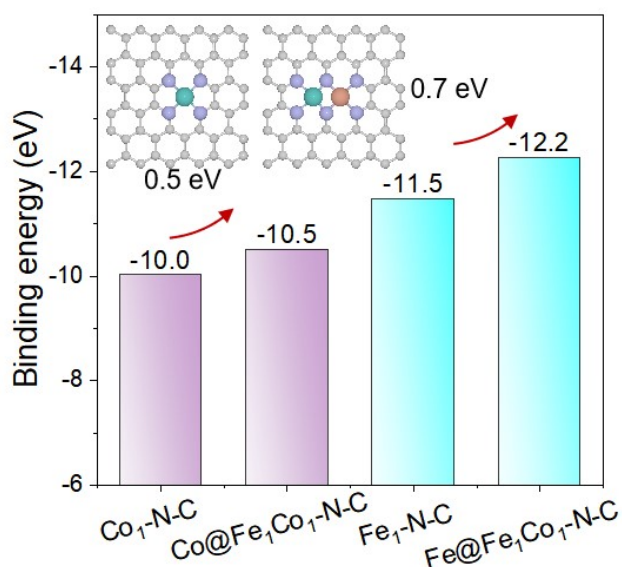


**Figure S4.** Comparison of binding energies of Co and Fe atoms in DAC or SAC structures.

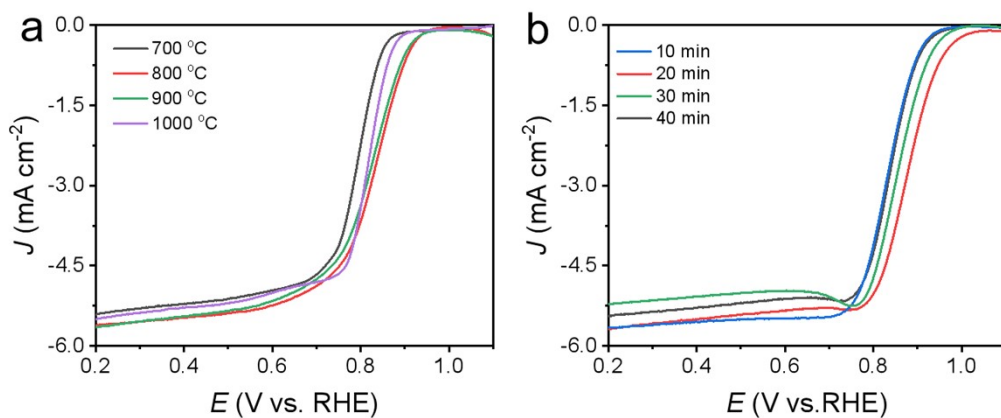


**Figure S5.** (a) LSV curves of the primary  $\text{Fe}_1\text{Co}_1\text{-N-C}$  catalysts at different pyrolysis temperatures without  $\text{CO}_2$  activation treatment. The optimal pyrolysis temperature is 800 °C. (b) LSV curves of the  $\text{Fe}_1\text{Co}_1\text{-N-C}$  catalysts prepared at 800 °C with different  $\text{CO}_2$  activation times. The optimal  $\text{CO}_2$  activation time is 20 min.

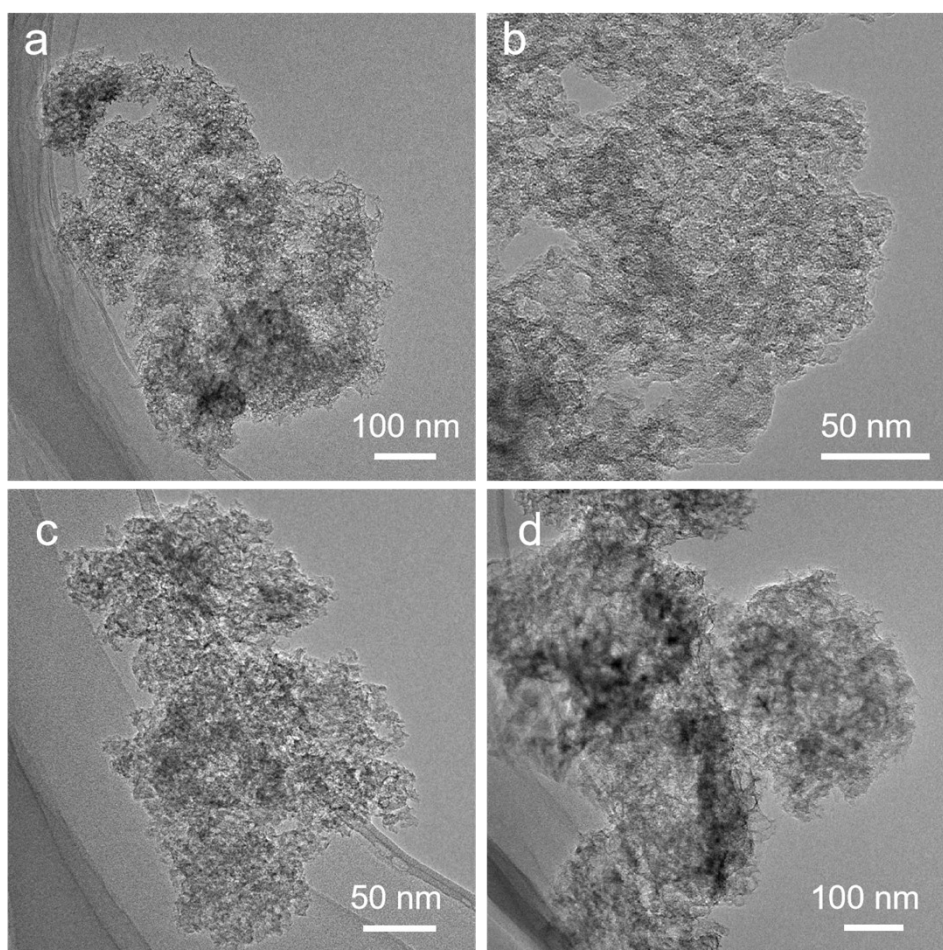


**Figure S6.** (a-d) TEM images of  $\text{Fe}_1\text{Co}_1\text{-N-C}$ .

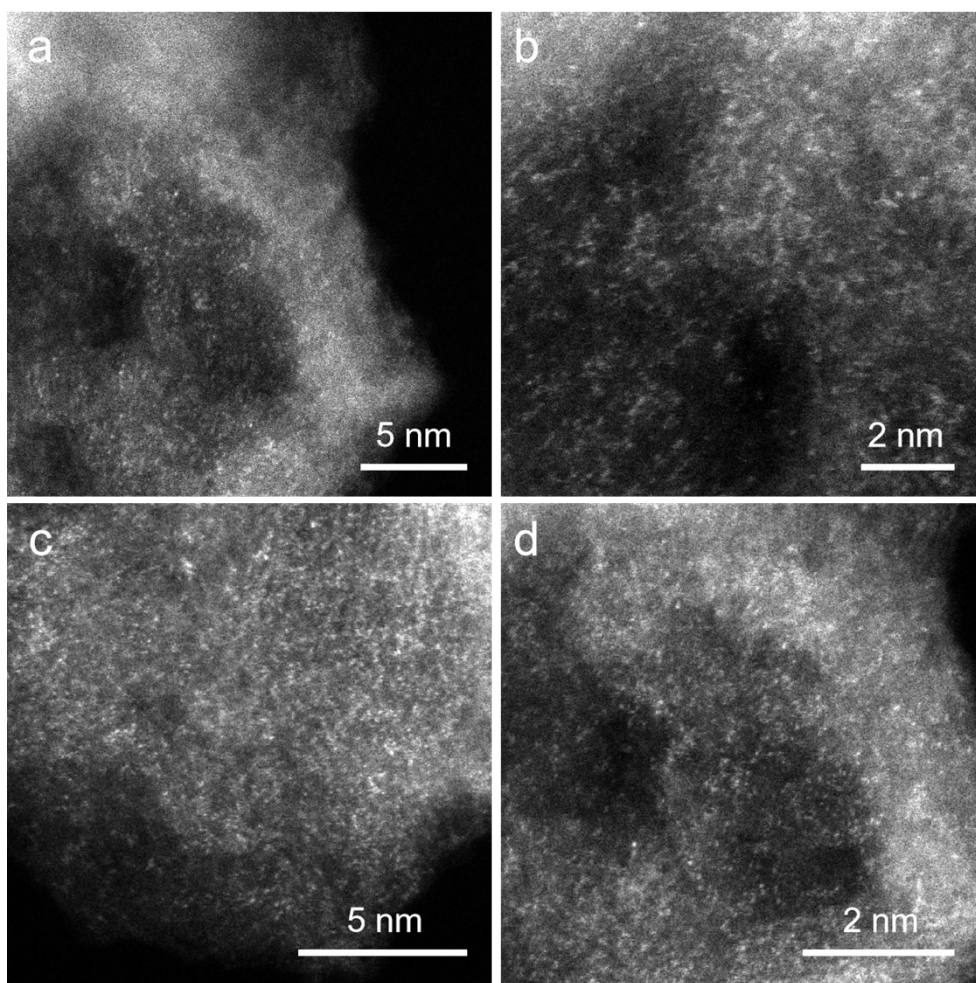


**Figure S7.** (a-d) HAADF-STEM images of  $\text{Fe}_1\text{Co}_1\text{-N-C}$ .

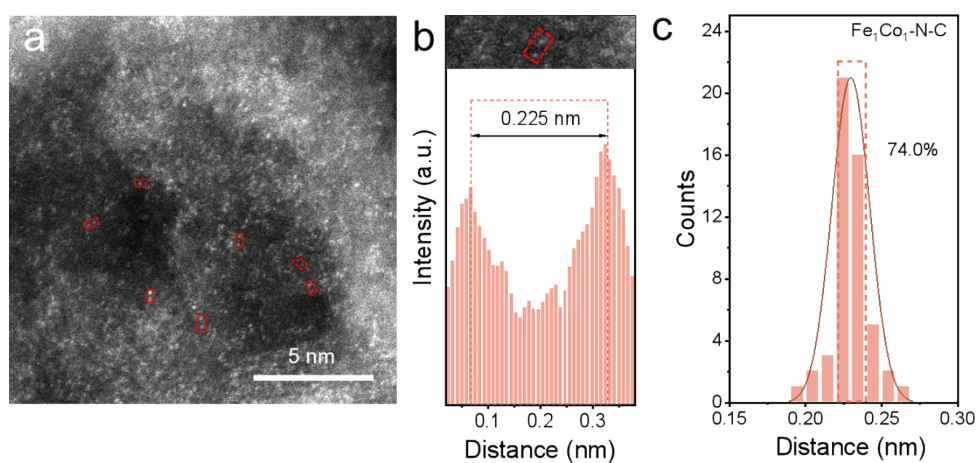


**Figure S8.** (a) HAADF-STEM image of  $\text{Fe}_1\text{Co}_1\text{-N-C}$  with Fe-Co dual atoms marked by red rectangles. (b) Randomly selected images in the red rectangle in (a). (c) Intensity profiles of dual-atom sites.

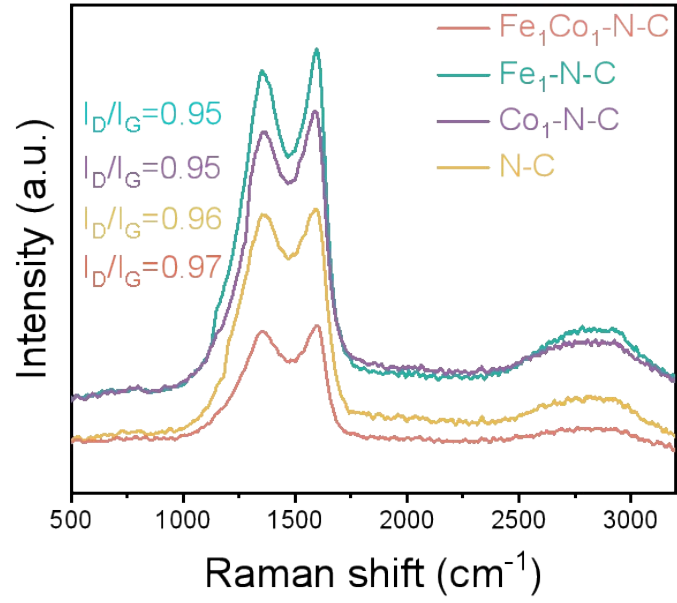


**Figure S9.** Raman spectra of Fe<sub>1</sub>Co<sub>1</sub>-N-C, Fe<sub>1</sub>-N-C, Co<sub>1</sub>-N-C, and N-C.

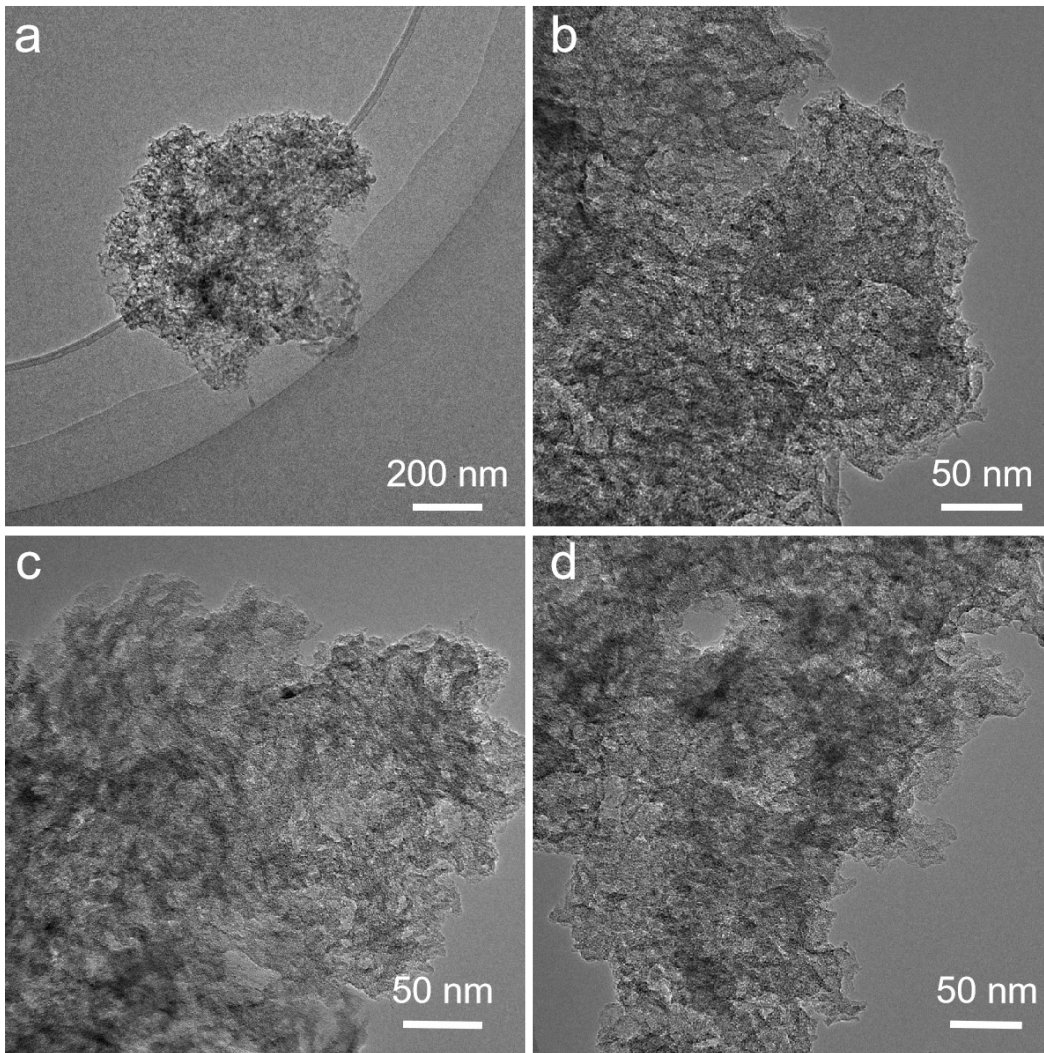


**Figure S10.** (a-d) TEM images of Fe<sub>1</sub>-N-C.

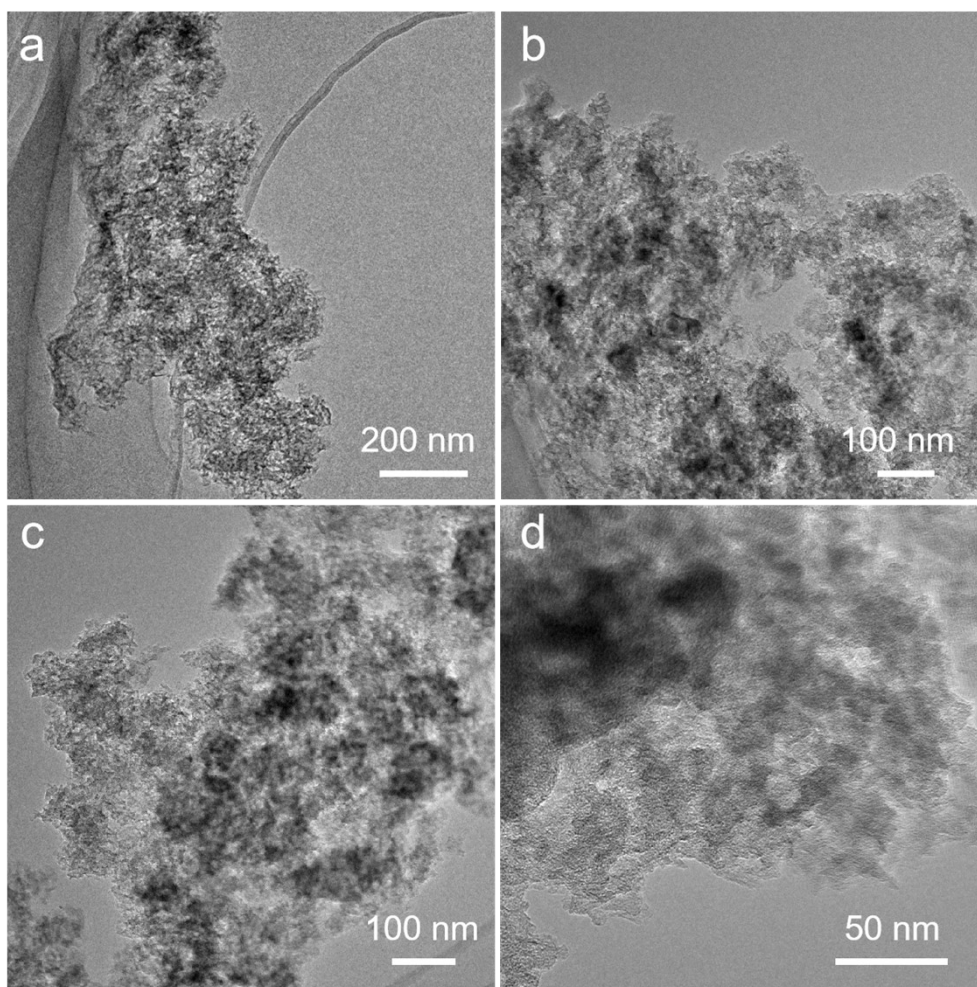


**Figure S11.** (a-d) TEM images of Co<sub>1</sub>-N-C.

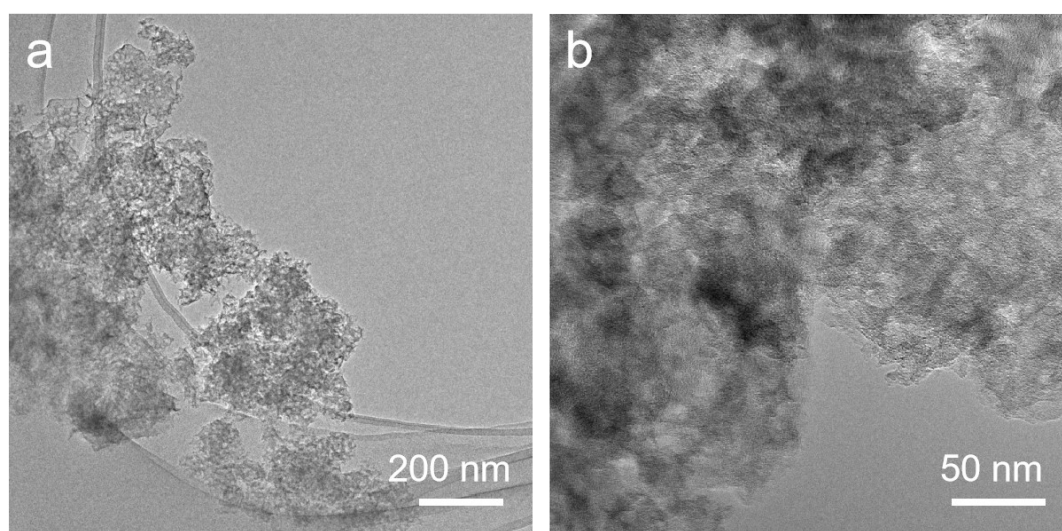


**Figure S12.** (a-b) TEM images of N-C.

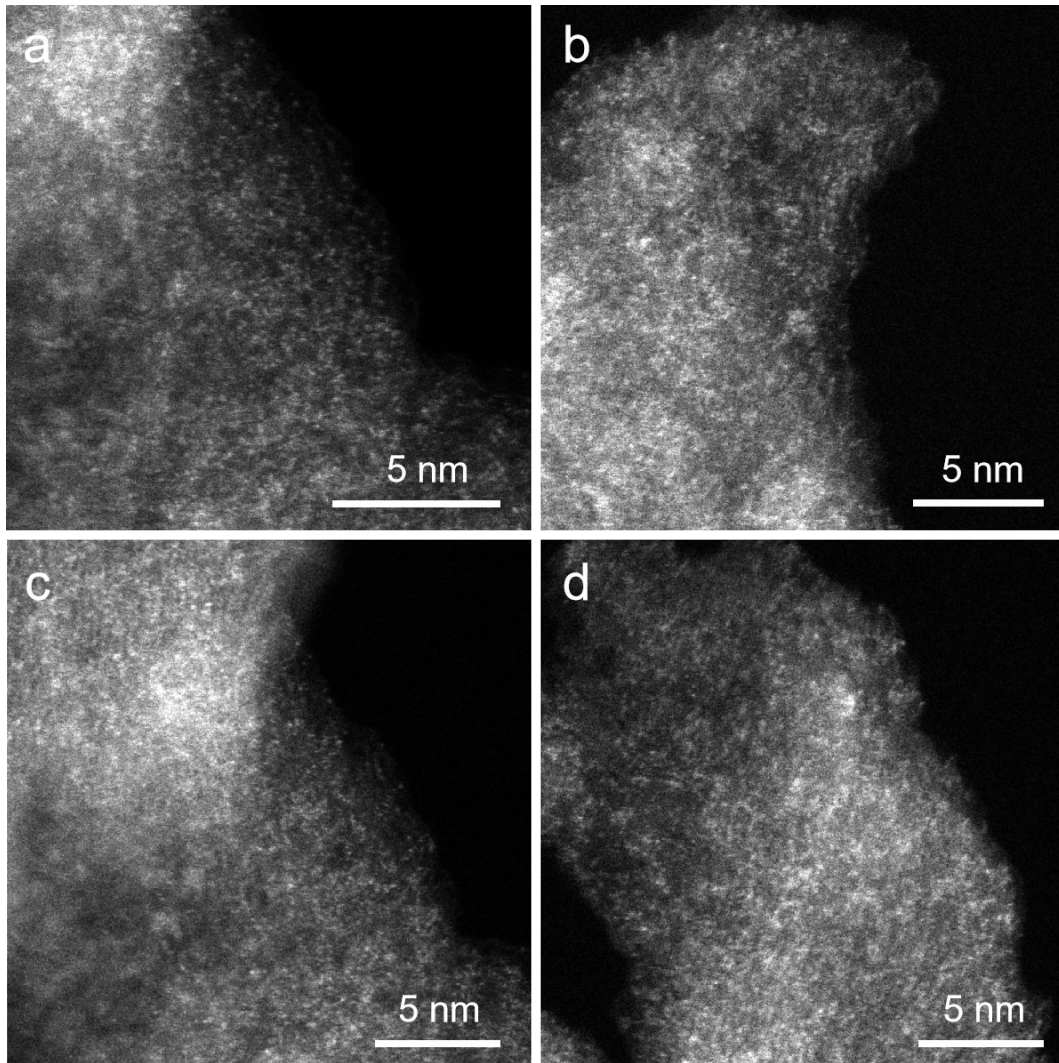


**Figure S13.** (a-d) HAADF-STEM images of Fe<sub>1</sub>-N-C.

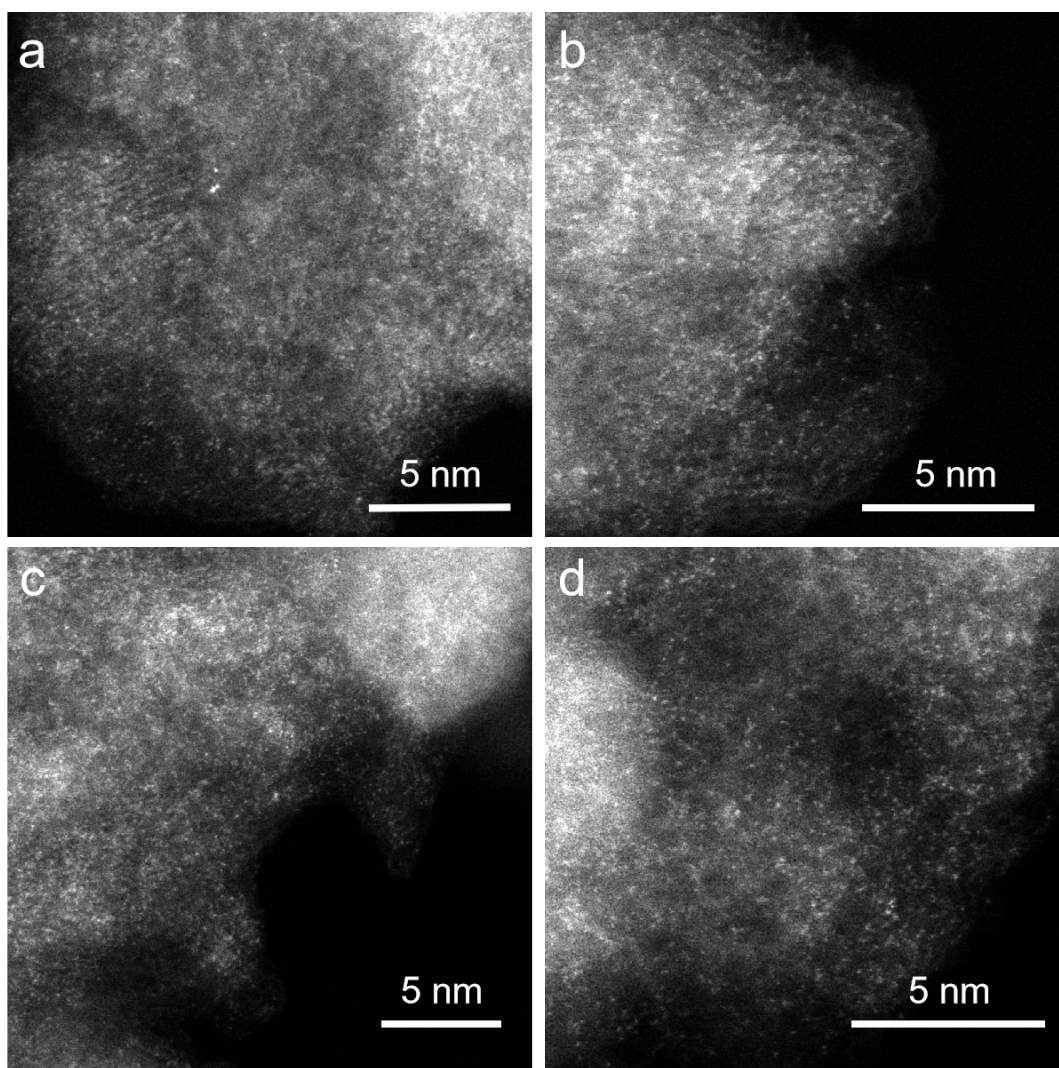


**Figure S14.** (a-d) HAADF-STEM images of  $\text{Co}_1\text{-N-C}$ .

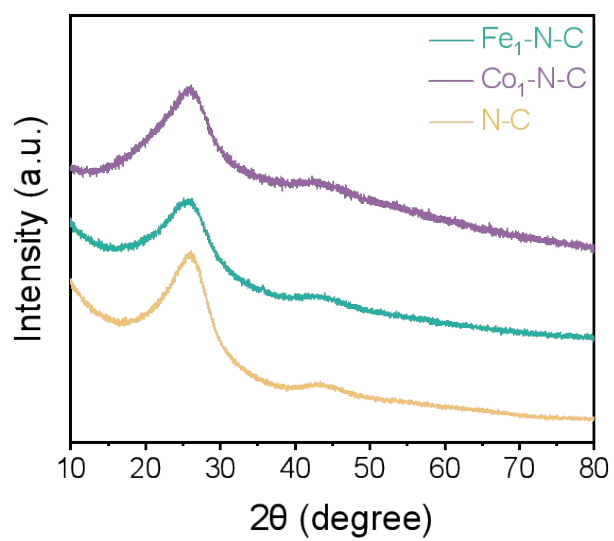


**Figure S15.** PXRD patterns of  $\text{Fe}_1\text{-N-C}$ ,  $\text{Co}_1\text{-N-C}$ , and  $\text{N-C}$ .

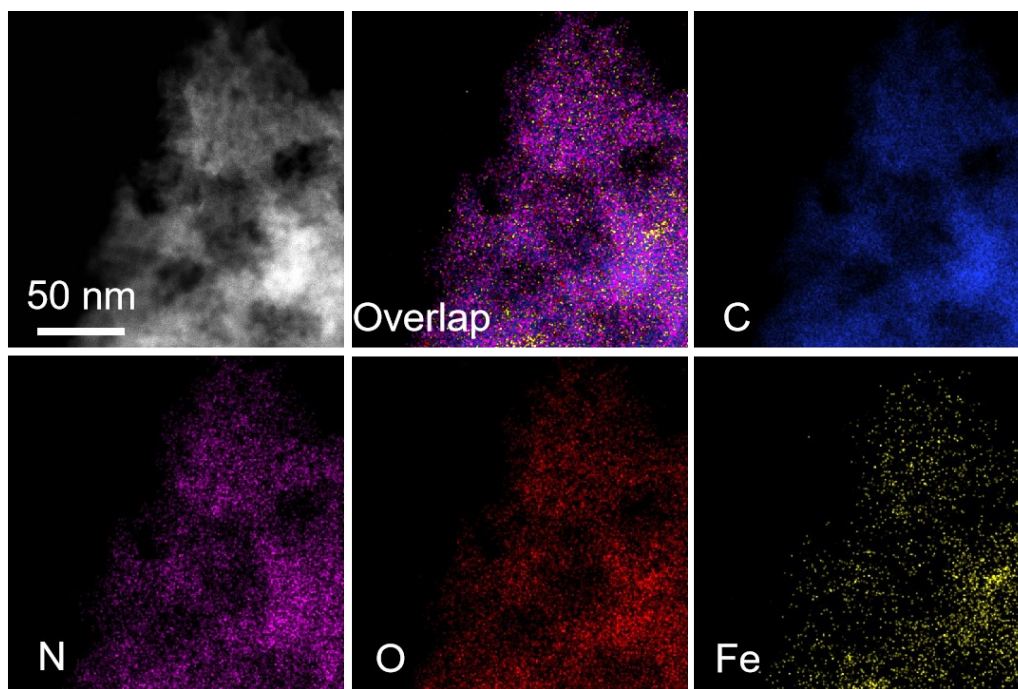


**Figure S16.** EDS mapping images of Fe<sub>1</sub>-N-C.

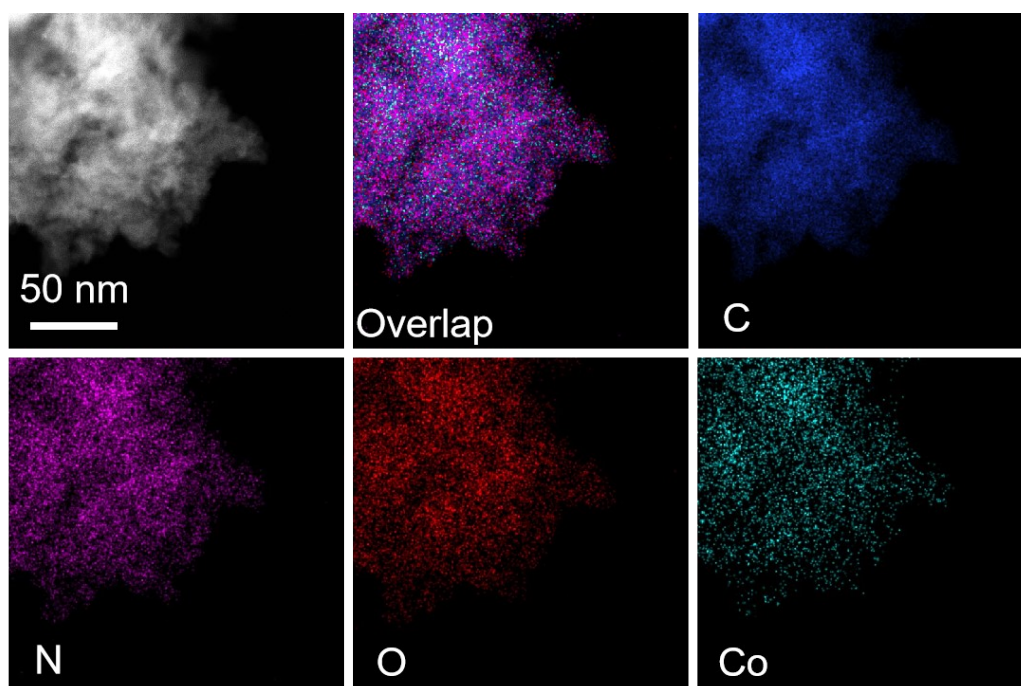


**Figure S17.** EDS mapping images of Co<sub>1</sub>-N-C.

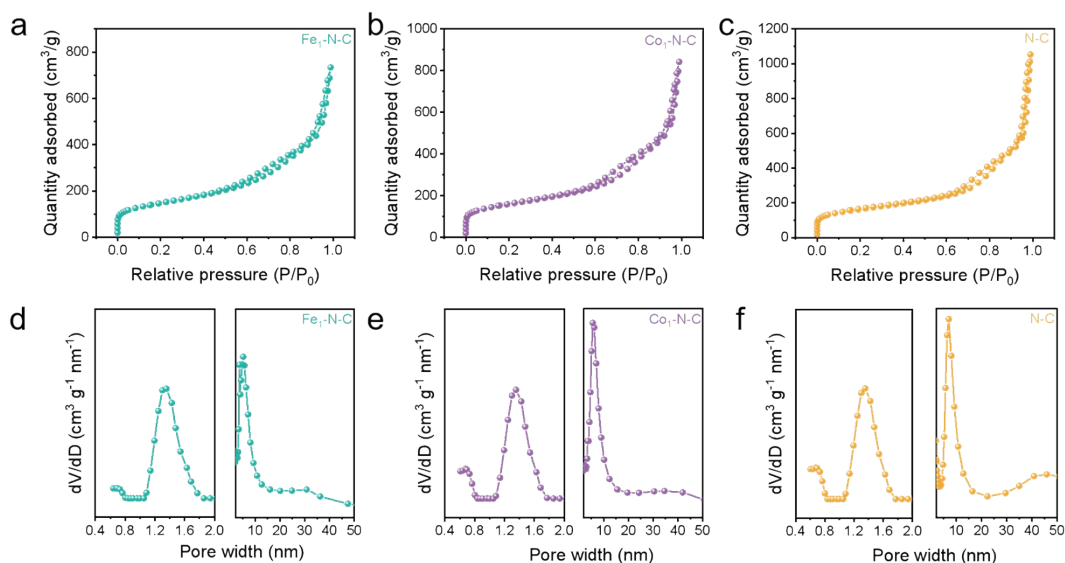


**Figure S18.** (a-c) N<sub>2</sub> adsorption/desorption isotherms, and (d-f) pore size distribution curves of Fe<sub>1</sub>-N-C, Co<sub>1</sub>-N-C, and N-C, respectively.

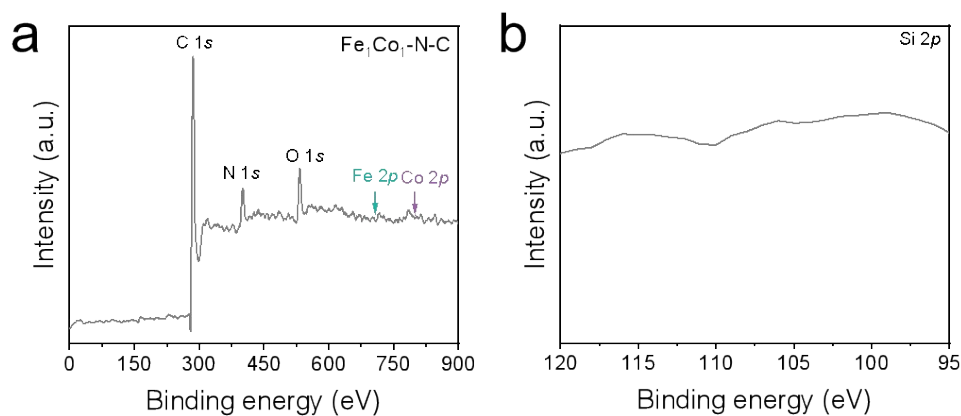


**Figure S19.** (a) XPS survey, and (b) Si 2p spectra of Fe<sub>1</sub>Co<sub>1</sub>-N-C.

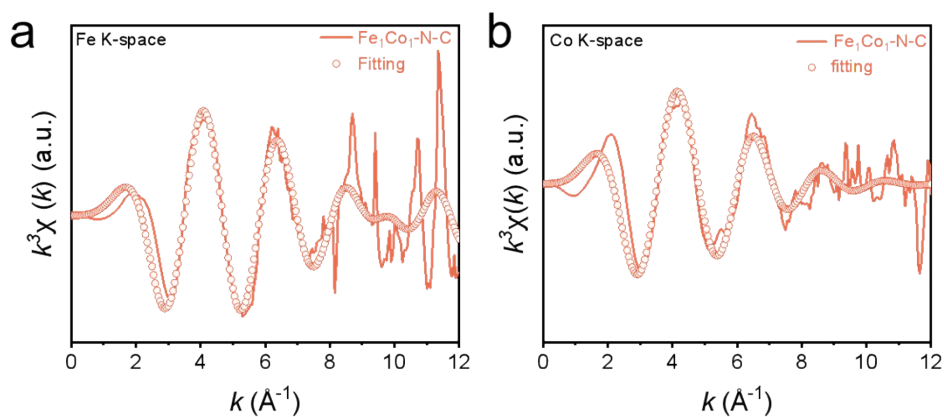


**Figure S20.** Corresponding (a) Fe, and (b) Co K-edge EXAFS fitting curves of Fe<sub>1</sub>Co<sub>1</sub>-N-C in K space.

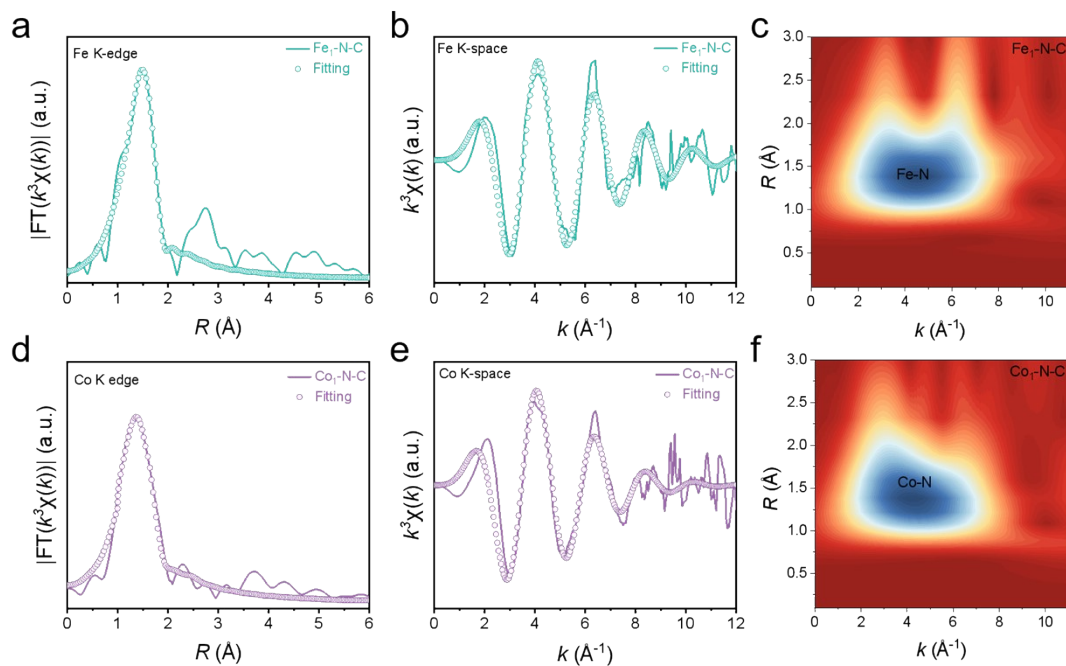


**Figure S21.** Corresponding Fe K-edge and Co K-edge EXAFS fitting curves of Fe<sub>1</sub>-N-C in (a)  $R$  space, and (b)  $K$  space and Co<sub>1</sub>-N-C in (d)  $R$  space, and (e)  $K$  space. (c, f) WT of  $\chi(k)$  of Fe for Fe<sub>1</sub>-N-C and Co for Co<sub>1</sub>-N-C.

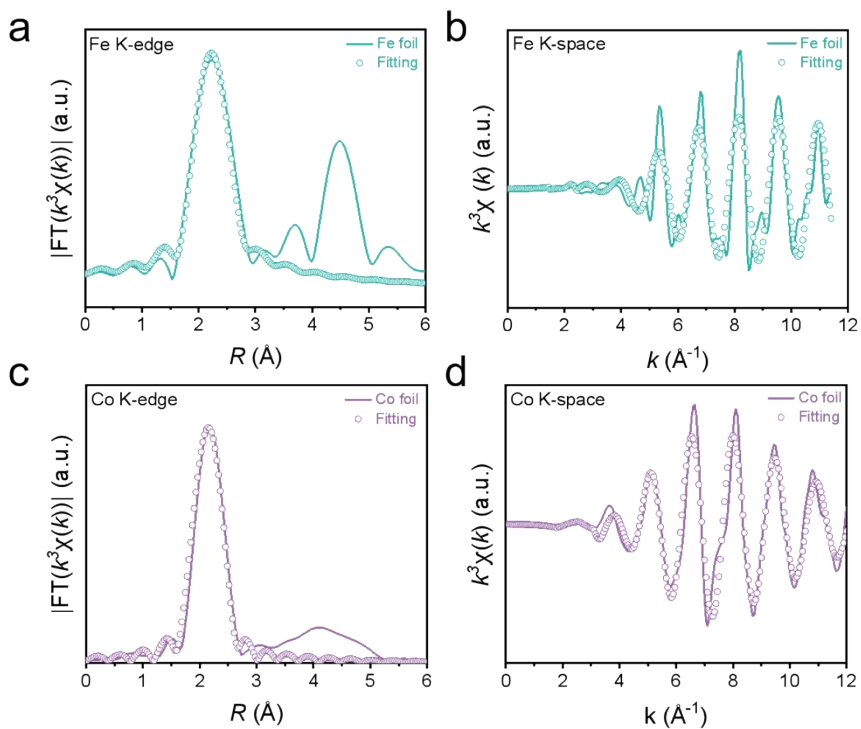


**Figure S22.** Fe K-edge and Co K-edge EXAFS fitting curves of Fe foil in (a)  $R$  space, and (b)  $K$  space and Co foil in (c)  $R$  space, and (d)  $K$  space.

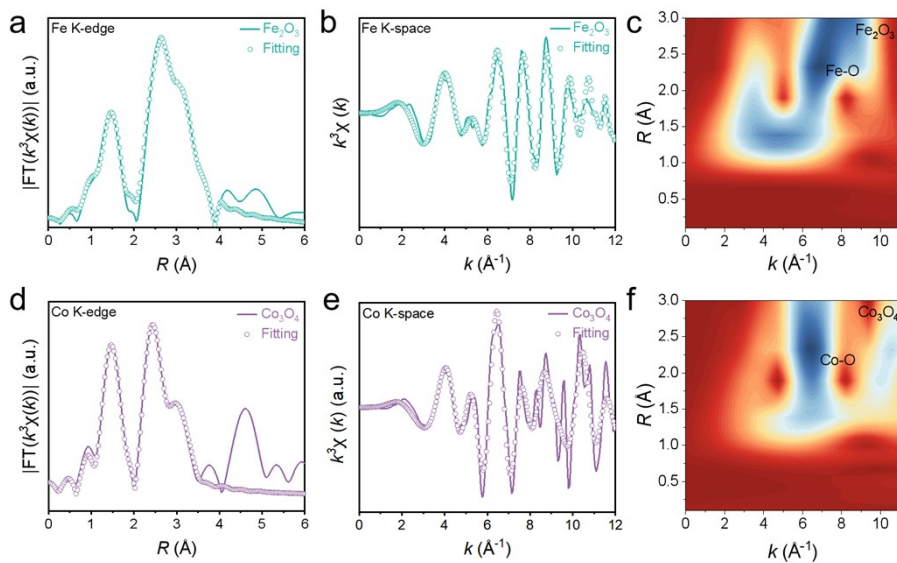


**Figure S23.** Corresponding Fe K-edge and Co K-edge EXAFS fitting curves of Fe<sub>2</sub>O<sub>3</sub> in (a) *R* space, (b) *K* space and Co<sub>3</sub>O<sub>4</sub> in (d) *R* space, and (e) *K* space. (c, f) WT of  $\chi(k)$  of Fe for Fe<sub>2</sub>O<sub>3</sub> and Co for Co<sub>3</sub>O<sub>4</sub>.

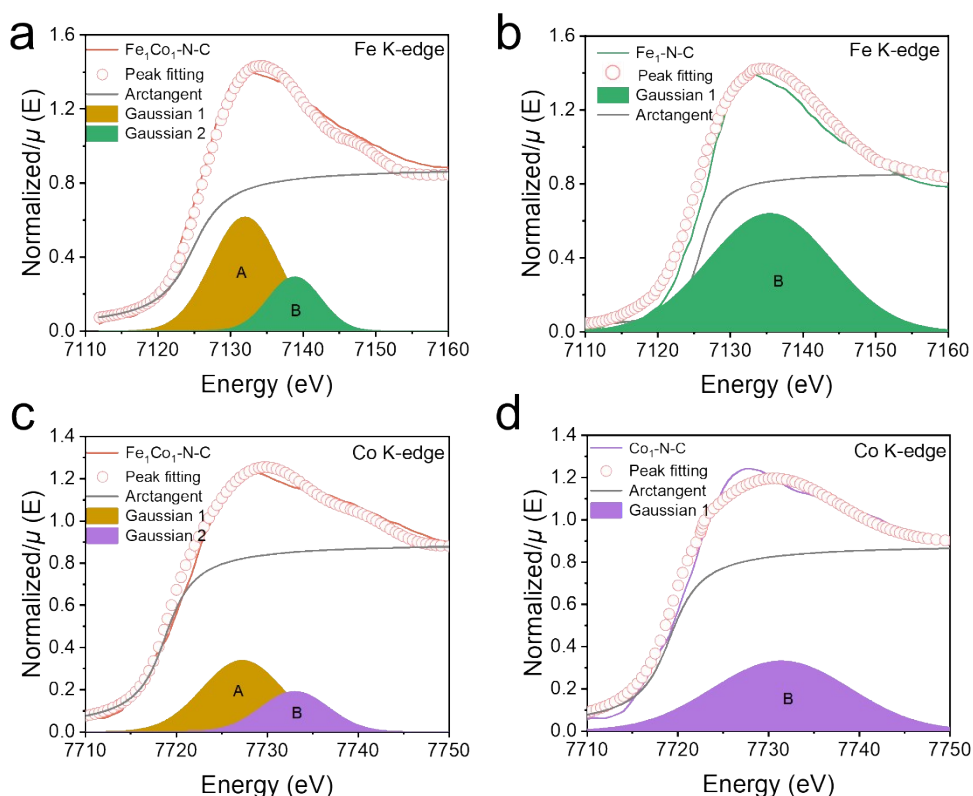


**Figure S24.** White line peak fitting analyses of Fe K-edge XANES spectra of (a) Fe<sub>1</sub>Co<sub>1</sub>-N-C, (b) Fe<sub>1</sub>-N-C, and Co K-edge XANES spectra of (c) Fe<sub>1</sub>Co<sub>1</sub>-N-C, (d) Co<sub>1</sub>-N-C.

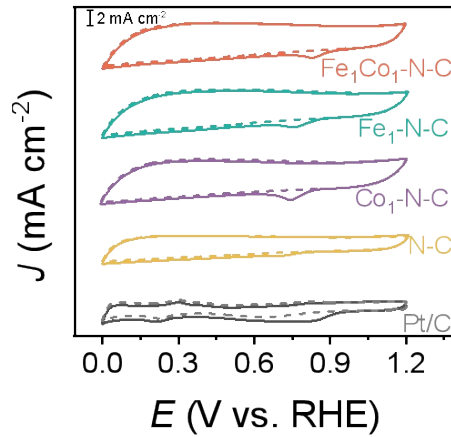


**Figure S25.** CV curves of Fe<sub>1</sub>Co<sub>1</sub>-N-C, Fe<sub>1</sub>-N-C, Co<sub>1</sub>-N-C, N-C, and Pt/C in Ar (dotted line) and O<sub>2</sub> (solid line) saturated 0.1 M KOH solutions.

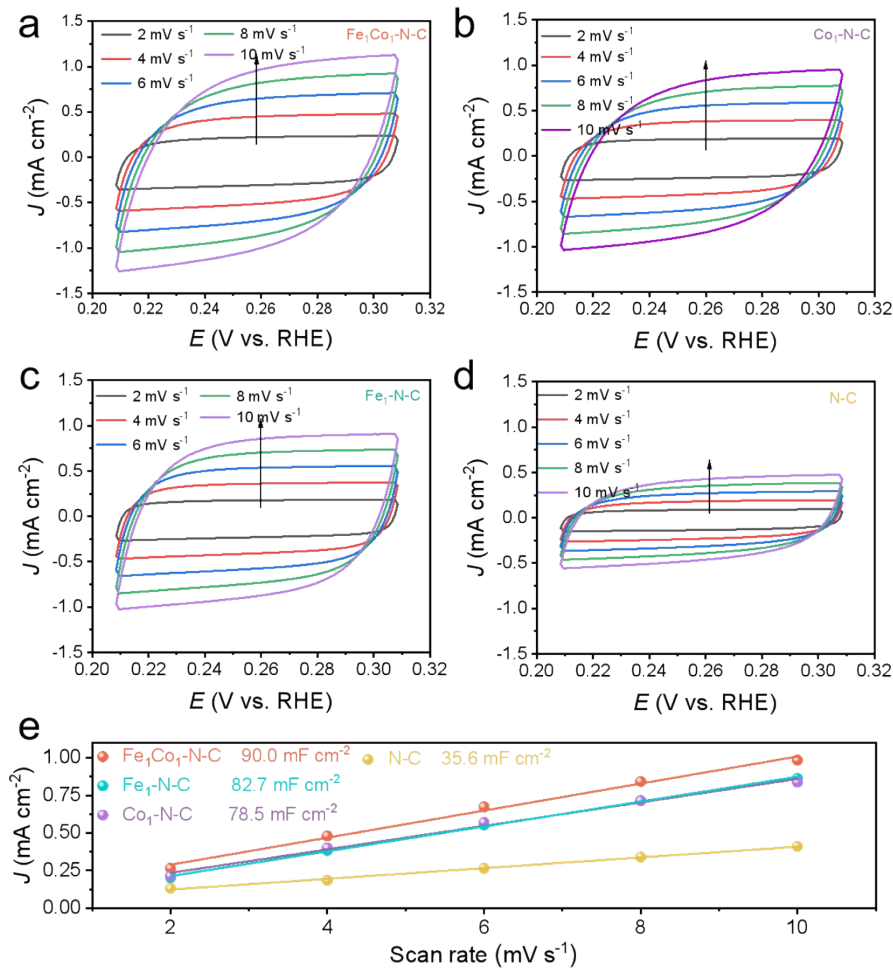


**Figure S26.** (a-d) CV curves in 0.1 M KOH solution showing the double layer capacitance in a non-Faradaic range of Fe<sub>1</sub>Co<sub>1</sub>-N-C, Fe<sub>1</sub>-N-C, Co<sub>1</sub>-N-C, and N-C. (e) Current densities at various scan rates for (a-d) and fitted to a linear regression for the estimation of capacitance.

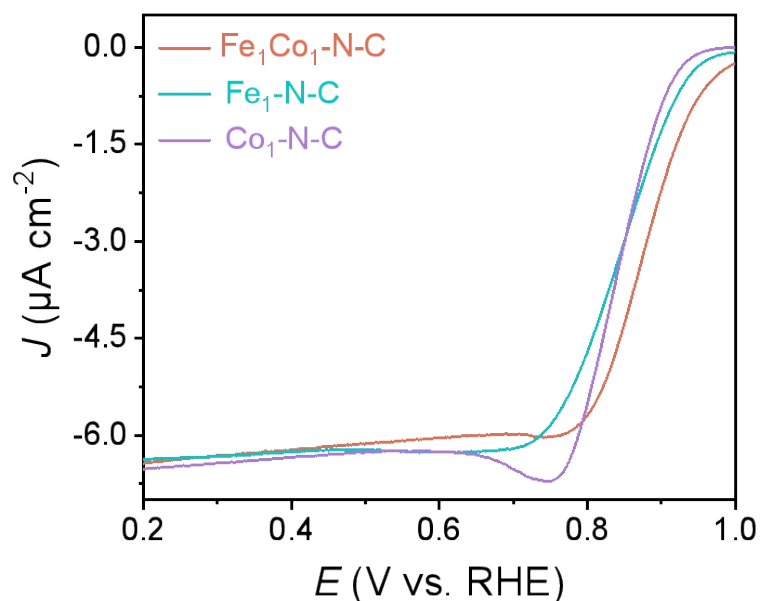


**Figure S27.** ECSA normalized LSV curves of Fe<sub>1</sub>Co<sub>1</sub>-N-C, Fe<sub>1</sub>-N-C, and Co<sub>1</sub>-N-C.

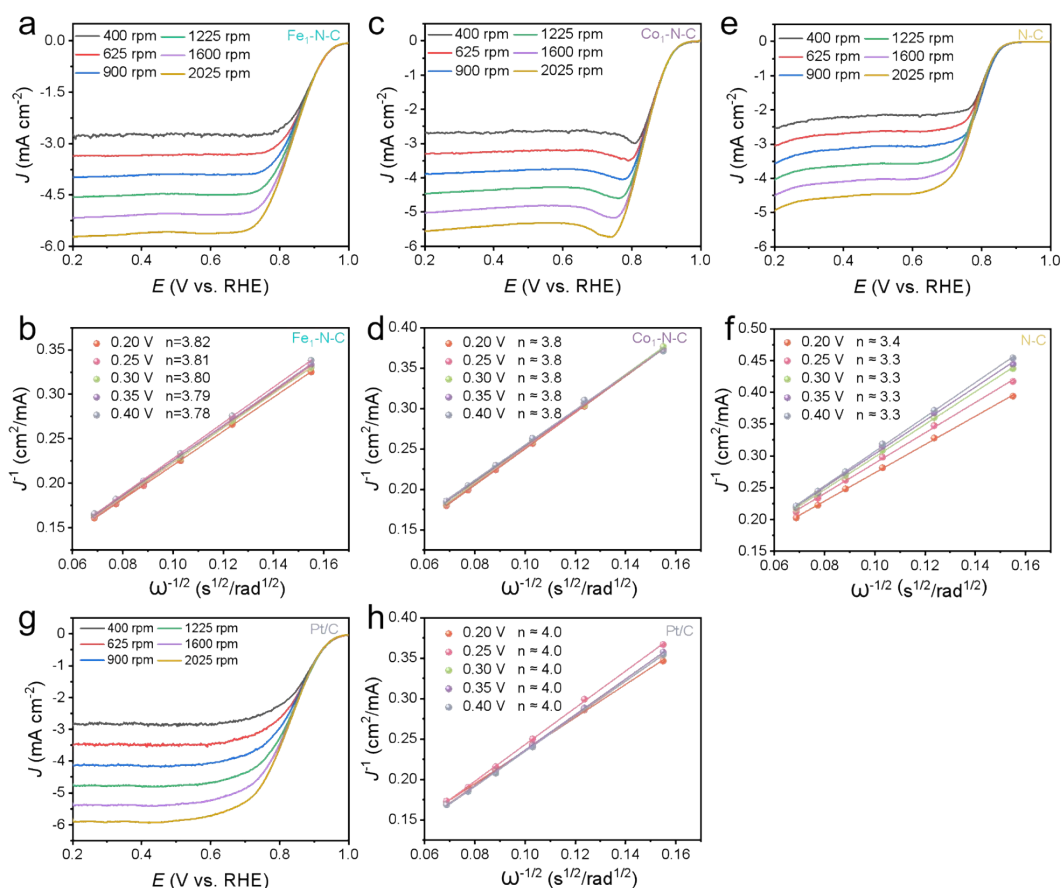


**Figure S28.** Polarization curves of (a) Fe<sub>1</sub>-N-C, (c) Co<sub>1</sub>-N-C, (e) N-C, and (g) Pt/C at different rotation speeds. (b, d, f, h) The corresponding K-L plots with electron transfer number (n) at different

potentials.

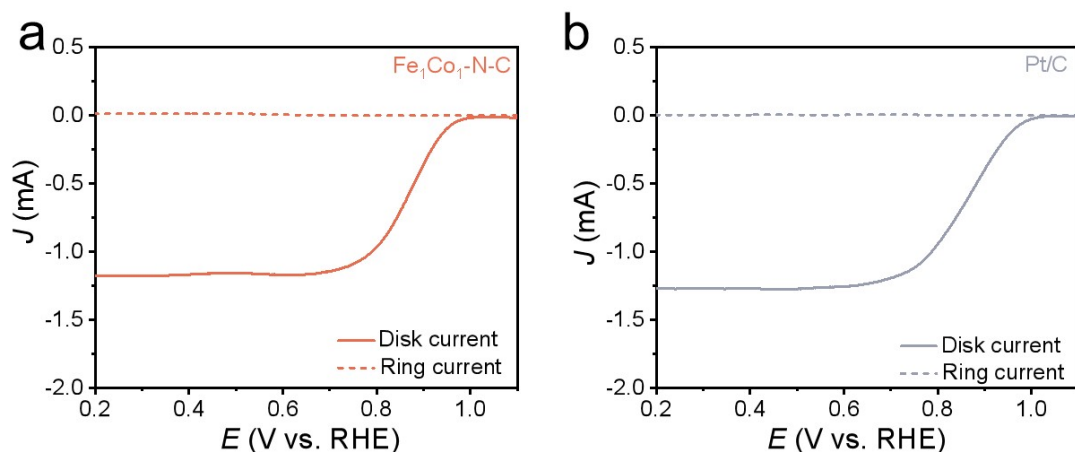


**Figure S29.** The RRDE polarization curves of (a) Fe<sub>1</sub>Co<sub>1</sub>-N-C and (b) Pt/C, respectively.

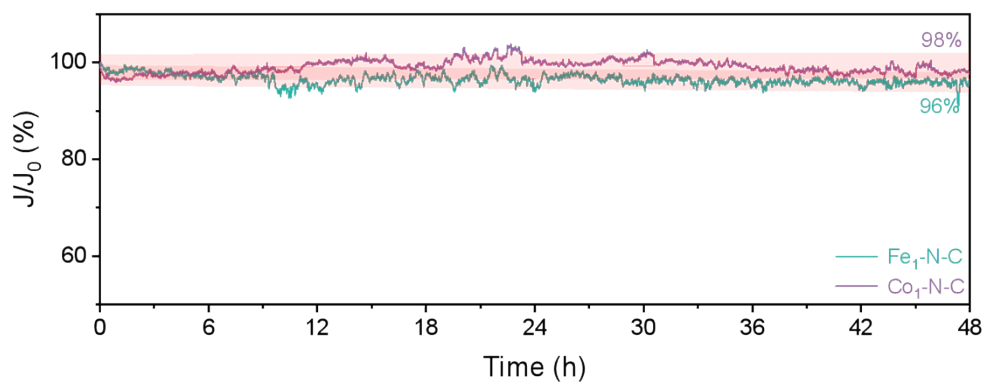


**Figure S30.** Normalized chronoamperometric curves of ORR for Fe<sub>1</sub>-N-C and Co<sub>1</sub>-N-C.

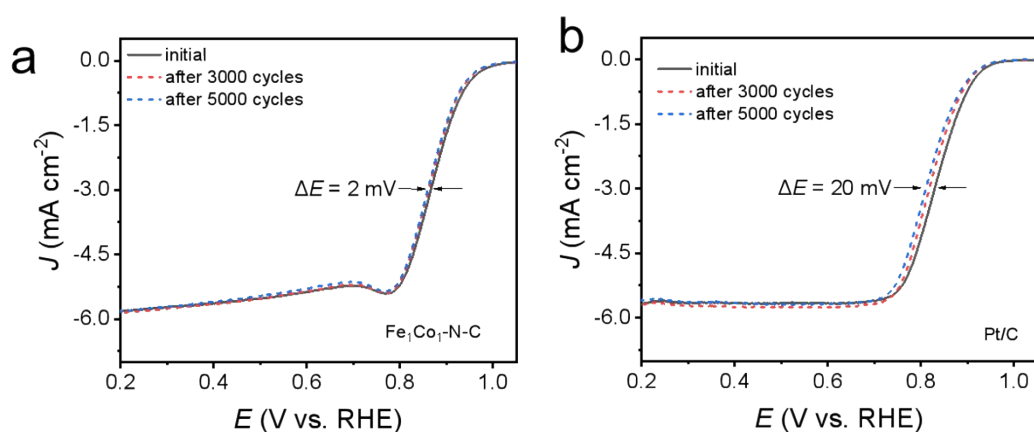


**Figure S31.** The ORR polarization curves of (a) Fe<sub>1</sub>Co<sub>1</sub>-N-C and (b) Pt/C before and after 5000 cycles between 0.7 and 0.9 V CV cycling.

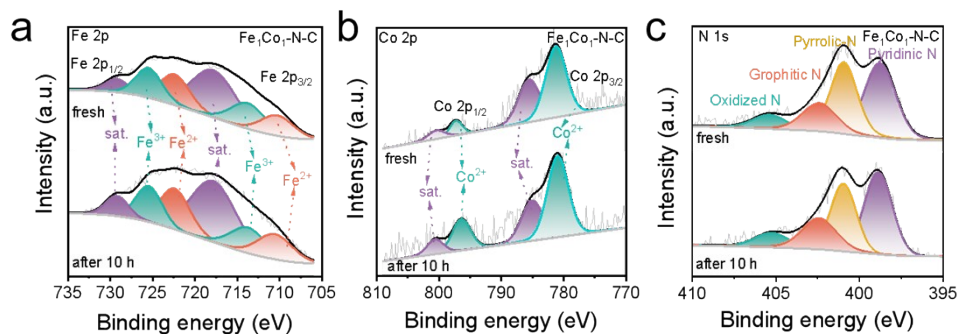


**Figure S32.** XPS results of Fe<sub>1</sub>Co<sub>1</sub>-N-C catalyst before and after 10 h of *i-t* measurements.

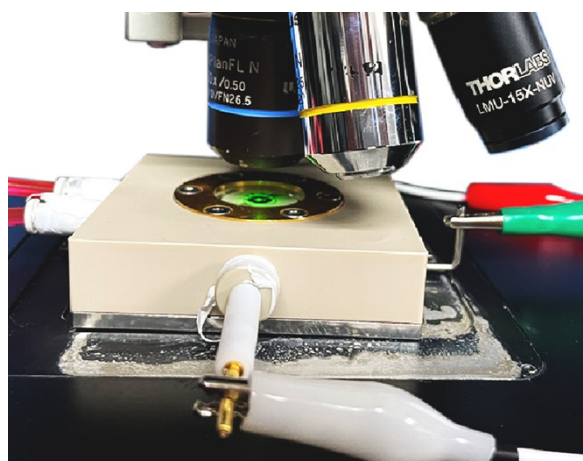


**Figure S33.** Optical image of Raman-electrochemical equipment.

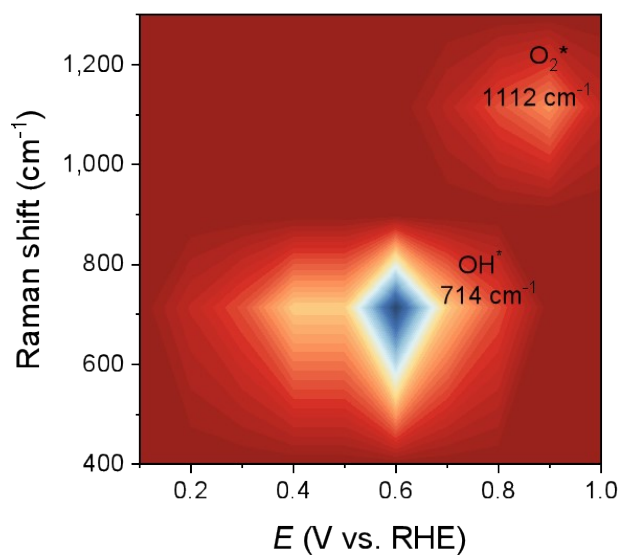


**Figure S34.** Potential dependence of the normalized peak area of in-situ Raman for O<sub>2</sub>\* (1112 cm<sup>-1</sup>) and HO\* (714 cm<sup>-1</sup>), respectively.

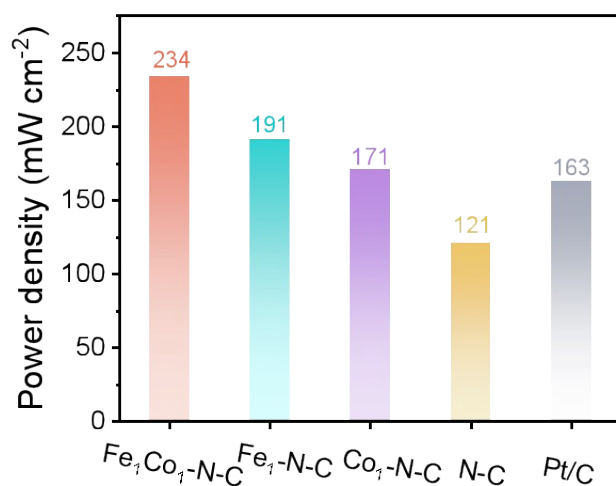


**Figure S35.** Power densities of ZABs using Fe<sub>1</sub>Co<sub>1</sub>-N-C, Fe<sub>1</sub>-N-C, Co<sub>1</sub>-N-C, N-C, and Pt/C as the air cathode catalysts.

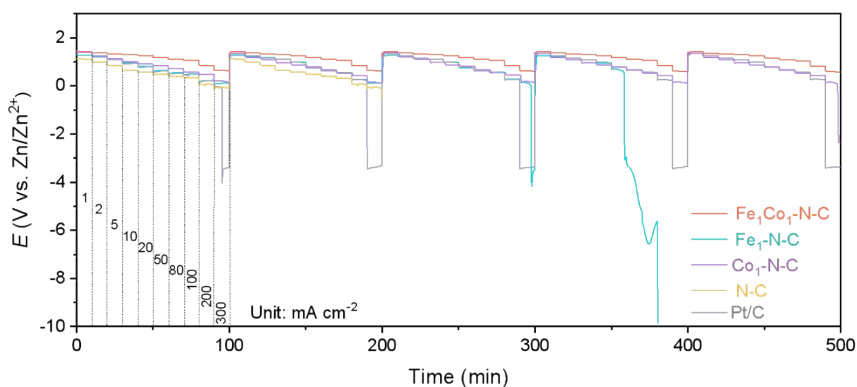


**Figure S36.** Discharge curves at current densities from 1 to 2, 5, 10, 20, 50, 80, 100, 200, 300 mA cm<sup>-2</sup> for 5 cycles of Fe<sub>1</sub>Co<sub>1</sub>-N-C, Fe<sub>1</sub>-N-C, Co<sub>1</sub>-N-C, N-C, and Pt/C as the air cathode.

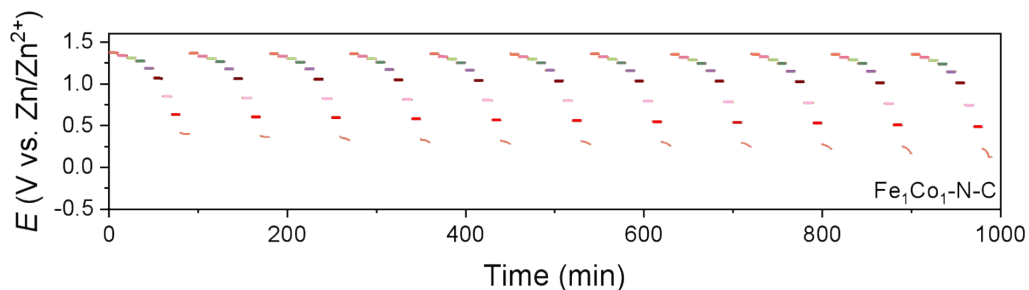


**Figure S37.** Discharge curves at current densities from 2 to 5, 10, 20, 50, 100, 300, 500, and 600 mA cm<sup>-2</sup> for 11 cycles of Fe<sub>1</sub>Co<sub>1</sub>-N-C.

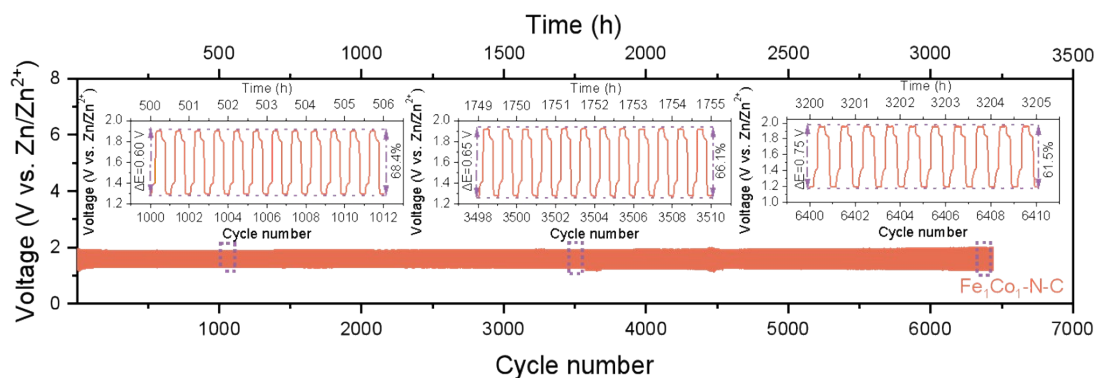


Figure S38. Cyclic stability at 5 mA cm<sup>-2</sup> current density for Fe<sub>1</sub>Co<sub>1</sub>-N-C based ZAB.

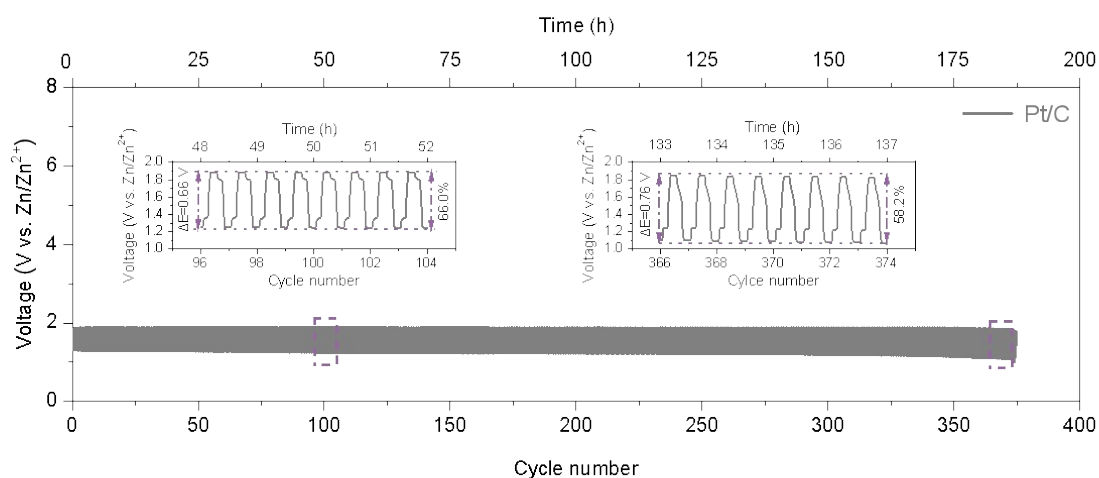


Figure S39. Cyclic stability at 5 mA cm<sup>-2</sup> using Pt/C as the air cathode for ZAB.

**Table S1.** Summary of the DFT-calculated energies, experimental Gibbs free formation energies, and entropic contributions at standard conditions: T = 298 K and pressure = 1 bar<sup>7</sup>. Unit: eV.

Species	$E^{\text{DFT}}$	ZPE	$T\Delta S^{\text{exp}}$	ZPE- $T\Delta S$	$E_{\text{solv}}$
H <sub>2</sub> O (l)	-14.1476	0.57	0.67 (0.035 bar)	-0.10	-
H <sub>2</sub> (g)	-6.9897	0.35	0.41	-0.06	-
O*	-	0.066	0	0.066	-
HO*	-	0.343	0	0.343	-0.15
HOO*	-	0.403	0	0.403	-0.40
O <sub>2</sub> *	-	0.135	0	0.135	-

**Table S2.** Summary of the adsorption free energy of different DACs and SACs.

Catalysts	Site	$G_{\text{HO}^*}$
Mn-N-C	Mn	0.39
Fe-N-C	Fe	0.61
Co-N-C	Co	0.94
Ni-N-C	Ni	1.93
Cu-N-C	Cu	1.80
Cu <sub>1</sub> Ni <sub>1</sub> -N-C	Ni site	1.994
	Cu site	2.052
Cu <sub>1</sub> Cu <sub>1</sub> -N-C	Cu site	1.960
	Cu site	1.975
Co <sub>1</sub> Ni <sub>1</sub> -N-C	Co site	1.495
	Ni site	2.046
Cu <sub>1</sub> Fe <sub>1</sub> -N-C	Fe site	1.298
	Cu site	1.284
Ni <sub>1</sub> Ni <sub>1</sub> -N-C	Ni site	1.945
	Ni site	2.081
Fe <sub>1</sub> Co <sub>1</sub> -N-C	Fe site	1.656
	Co site	1.565
Fe <sub>1</sub> Fe <sub>1</sub> -N-C	Fe site	1.585
	Fe site	1.609

Co <sub>1</sub> Co <sub>1</sub> -N-C	Co site	1.599
	Co site	1.736
Cu <sub>1</sub> Co <sub>1</sub> -N-C	Co site	1.411
	Cu site	1.806
Fe <sub>1</sub> Ni <sub>1</sub> -N-C	Ni site	1.768
	Fe site	1.192

**Table S3.** Barder charge analysis of SACs and DACs.

Sample	Charge (e)	Loss charge (e)	E <sub>HO*</sub>
Fe <sub>1</sub> -N-C	6.88	1.12	0.61
Co <sub>1</sub> -N-C	8.11	0.89	0.84
Fe site in Fe <sub>1</sub> Co <sub>1</sub> -N-C	7.0	1.0	1.66
Co site in Fe <sub>1</sub> Co <sub>1</sub> -N-C	8.13	0.87	1.56

**Table S4.** ORR performance of the primary Fe<sub>1</sub>Co<sub>1</sub>-N-C electrocatalysts as a function of the pyrolysis temperature but without CO<sub>2</sub> activation treatment.

Sample	E <sub>onset</sub> (V vs. RHE)	E <sub>1/2</sub> (V vs. RHE)	Current density at 0.4 V (mA cm <sup>-2</sup> )
Fe <sub>1</sub> Co <sub>1</sub> -N-C-700	0.964	0.796	-5.22
Fe <sub>1</sub> Co <sub>1</sub> -N-C-800	0.970	0.833	-5.47
Fe <sub>1</sub> Co <sub>1</sub> -N-C-900	0.970	0.825	-5.45
Fe <sub>1</sub> Co <sub>1</sub> -N-C-1000	0.935	0.817	-5.30

**Table S5.** ORR performance of the Fe<sub>1</sub>Co<sub>1</sub>-N-C electrocatalysts as a function of the CO<sub>2</sub> activation time. The pyrolysis temperature is 800 °C.

Sample	$E_{\text{onset}}$ (V vs. RHE)	$E_{1/2}$ (V vs. RHE)	Current density at 0.4 V (mA cm <sup>-2</sup> )
Fe <sub>1</sub> Co <sub>1</sub> -N-C-800-10	0.952	0.834	-5.57
Fe <sub>1</sub> Co <sub>1</sub> -N-C-800-20	1.000	0.882	-5.57
Fe <sub>1</sub> Co <sub>1</sub> -N-C-800-30	0.984	0.861	-5.07
Fe <sub>1</sub> Co <sub>1</sub> -N-C-800-40	0.961	0.841	-5.28

**Table S6.** Metal elemental contents of Fe, Co containing samples determined by using ICP-MS test.

Fe <sub>1</sub> Co <sub>1</sub> -N-C		Fe <sub>1</sub> -N-C	Co <sub>1</sub> -N-C
Fe	Co	Fe	Co
1.00 wt%	1.40 wt%	1.63 wt%	3.35 wt%

**Table S7.** BET surface area and pore volume of the as-prepared Fe<sub>1</sub>Co<sub>1</sub>-N-C, Fe<sub>1</sub>-N-C, Co<sub>1</sub>-N-C, and N-C.

Sample	$S_{\text{BET}}$ (m <sup>2</sup> g <sup>-1</sup> )	Pore volume (cm <sup>3</sup> g <sup>-1</sup> )
Fe <sub>1</sub> Co <sub>1</sub> -N-C	531.5	0.84
Fe <sub>1</sub> -N-C	505.5	1.07
Co <sub>1</sub> -N-C	538.6	1.22
N-C	550.5	1.54

**Table S8.** The structural parameters were extracted from the Fe K-edge EXAFS fitting.

Sample	shell	CN	$R(\text{\AA})$	$\sigma^2 (\text{\AA}^2)$	$E_0$ (eV)	$R$ factor
Fe <sub>1</sub> Co <sub>1</sub> -N-C	Fe-N	4.2	2.04	0.004	5.72	0.01
Fe <sub>1</sub> -N-C	Fe-N	4.1	1.99	0.02	4.75	0.001
Fe <sub>2</sub> O <sub>3</sub>	Fe-O	3	2.0	0.04	1.05	0.04
	Fe-Fe	3	2.84	0.008	0.97	
Fe foil	Fe-Fe <sub>1</sub>	8	2.47	0.005	5.57	0.04
	Fe-Fe <sub>2</sub>	6	2.84	0.005	5.57	

CN: coordination numbers;  $R$ : bond distance;  $\sigma^2$ : Debye-Waller factors;  $E_0$ : the inner potential correction.  $R$  factor: goodness of fit. \*The experimental EXAFS fit of metal foil by fixing CN as the known crystallographic value.

**Table S9.** The structural parameters were extracted from the Co K-edge EXAFS fitting.

Sample	shell	CN	$R(\text{\AA})$	$\sigma^2 (\text{\AA}^2)$	$E_0$ (eV)	$R$ factor
Fe <sub>1</sub> Co <sub>1</sub> -N-C	Co-N	4.1	1.93	0.02	8.99	0.01
Co <sub>1</sub> -N-C	Co-N	3.9	1.97	0.02	8.17	0.008
Co <sub>3</sub> O <sub>4</sub>	Co-O	3	1.91	0.002	7.79	0.001
	Co-Co	6	2.87	0.006	7.79	
Co foil	Co-Co	12	2.49	0.02	8.16	0.005

**Table S10.** Comparison of ORR performance for Fe<sub>1</sub>Co<sub>1</sub>-N-C with reported performance of SACs and DACs electrocatalysts in alkaline electrolyte.

Catalysts	$E_{\text{onset}}$ (V vs. RHE)	$E_{1/2}$ (V vs. RHE)	Stability (CV cycle/ <i>i-t</i> )	Ref.
<b>Fe<sub>1</sub>Co<sub>1</sub>-N-C</b>	<b>1.0</b>	<b>0.882</b>	<b>5000 cycles; 48 h</b>	<b>This work</b>
Fe-N-C	0.903	0.987	-	22
Co-N-C	0.99	0.87	5000 cycles	23
Zn/Co-N-C	1.004	0.861	10000 cycles	24
Fe-N <sub>4</sub> & Co-N <sub>4</sub>	0.98	0.86	35000 s	25
Fe-N-C	0.95	0.88	-	26
CNT-O@Co	0.95	0.77	18 h	27
Ni-N <sub>4</sub> /GHSs/Fe-N <sub>4</sub>	0.93	0.83	-	28
Fe/Meso-NC-1000	0.97	0.885	3000 cycles	29
CoNC SAC	0.93	0.86	-	30
FeCo-NPC	0.96	0.83	30000 s	31
FePc/CoPc HS	0.971	0.879	5000 s	32
Fe-NHC	0.94	0.89	9 h	33
Cu/Zn-N-C	0.98	0.83	10000 cycles	34
CoSA+Co <sub>9</sub> S <sub>8</sub> /HCNT	0.9	0.855	-	35
CoNi-SAs/NC	0.88	0.76	10 h	36
W SAs/WNNC-5	0.89	0.83	16 h	37
FeMnCoNiCu-N-C	0.92	0.84	1000	38
Fe-N-C	1	0.87	12 h	39
Fe-N/G-Co	0.97	0.85	10000 cycles; 50 h	40

FeSA/N-PSCS	0.976	0.87	5000 cycles	41
-------------	-------	------	-------------	----

**Table S11.** Comparison of OCV and maximum peak power density for Fe<sub>1</sub>Co<sub>1</sub>-N-C, Fe<sub>1</sub>-N-C, Co<sub>1</sub>-N-C, N-C, and Pt/C electrocatalysts in ZABs.

Sample	OCV (V vs. Zn/Zn <sup>2+</sup> )	Maximum peak power density (mW cm <sup>-2</sup> )
Fe <sub>1</sub> Co <sub>1</sub> -N-C	1.51	234
Fe <sub>1</sub> -N-C	1.48	191
Co <sub>1</sub> -N-C	1.46	170
N-C	1.38	121
Pt/C	1.47	163

**Table S12.** Comparison of ZAB performance of the Fe<sub>1</sub>Co<sub>1</sub>-N-C catalyst based ZAB with recent reported catalysts based ZABs.

Catalyst	OCV	Power density (mW cm <sup>-2</sup> )	Cycling stability (h/cycles)	Maximum discharge current density (mA cm <sup>-2</sup> )	Ref.
<b>Fe<sub>1</sub>Co<sub>1</sub>-N-C</b>	<b>1.51</b>	<b>234</b>	<b>Over 3600 h (7244 cycles)</b>	<b>600</b>	<b>This work</b>
Co-SAs/SNPs@NC	1.493	223.5	720 h (1030 cycles)	50	42
PtFeNi	1.45	175	500 h	100	43
Fe-Co-Ni MOF	1.424	161	130 h (700 cycles)	50	44
Fe <sub>2</sub> N <sub>6</sub> -S	1.49	200.1	400 h (800 cycles)	50	45
Fe-Se/NC	1.47	135	200 h (1090 cycles)	50	46

{Co <sup>II</sup> }-300	1.45	134.49	1742 h (3485 cycles)	20	47
SSM/Co <sub>4</sub> N/CoNC	-	105	3350 h (10000 cycles)	20	48
NiFe-N-C	1.59	153.04	750 h (3600 cycles)	50	49
Co-SAs/N-C/rGO	1.52	104.91	10 h	100	50
Fe-N/P-C	1.42	133.2	40 h	100	51
FePc- {PW12}@CNT	1.39	280	500 h (500 cycles)	20	52
FeCo-NPC	1.49	301.4	200 h (600 cycles)	200	53
Ni SAs-NC	1.43	165	300 h (300 cycles)	100	54
FeNC@LDH	-	176	607 cycles	50	55
Co/SP-NC	1.46	187	280 h	50	56
CoCNTs/PNAs	1.51	371.5	43.3 h (260 cycles)	50	57
FeOCo-SAD	1.52	241.24	45 h	50	58
Co/DACN	1.57	210.1	2336 h (7000 cycles)	200	59
Au SAC CoN@NF	1.38	161.94	260 h (250 cycles)	100	60
CoFeCu-TAC	1.538	208	1970 h (3940 cycles)	20	61
CoSAs@NC-920	1.425	166	155 h	50	62
g-Cu-SACs	1.48	112	650 h	50	63

**Note S1.** The discussion of successful synthesis of Fe<sub>1</sub>-N-C, Co<sub>1</sub>-N-C, and N-C catalysts.

Fe<sub>1</sub>-N-C, Co<sub>1</sub>-N-C, and N-C were also prepared for comparison in this study. The content of Fe and Co determined by ICP-MS analysis are 1.63 and 3.35 wt%, respectively (**Table S6, ESI†**). TEM observations and N<sub>2</sub> sorption analysis reveal the hierarchical porous structure of Fe<sub>1</sub>-N-C, Co<sub>1</sub>-N-C, and N-C (**Figs. S8-10 and S16, ESI†**). Their BET surface area and pore volume are summarized in **Table S7, ESI†**. HAADF-STEM images indicate the Fe<sub>1</sub>-N-C and Co<sub>1</sub>-N-C have single-atom dispersed sites (**Figs. S11 and S12, ESI†**). Raman and PXRD spectra indicate the graphitic carbon structures of Fe<sub>1</sub>-N-C, Co<sub>1</sub>-N-C, and N-C (**Figs. S7 and S13, ESI†**). EDS mapping analysis for Fe<sub>1</sub>-N-C and Co<sub>1</sub>-N-C shows that Fe and Co are atomically dispersed on N-doped carbon (**Figs. S14 and S15, ESI†**). All of these characterizations clearly indicate that Fe<sub>1</sub>-N-C, Co<sub>1</sub>-N-C, and N-C with very similar structure properties to the Fe<sub>1</sub>Co<sub>1</sub>-N-C had been successfully prepared.

## Reference

1. B. Hammer, L.B. Hansen and J.K. Nørskov, *Phys. Rev. B* 1999, **59**, 7413-7421.
2. J.P. Perdew, K. Burke and M. Ernzerhof, *Phys. Rev. Lett.* 1996, **77**, 3865-3868.
3. P.E. Blöchl, *Phys. Rev. B* 1994, **50**, 17953-17979.
4. W. Kohn and L.J. Sham, *Phys. Rev.* 1965, **140**, A1133-A1138.
5. A.H. Larsen, J.J. Mortensen, J. Blomqvist, I.E. Castelli, R. Christensen, M. Dułak, J. Friis, M.N. Groves, B. Hammer, C. Hargus, E.D. Hermes, P.C. Jennings, P.B. Jensen, J. Kermode, J.R. Kitchin, E.L. Kolsbjerg, J. Kubal, K. Kaasbjerg, S. Lysgaard, J.B. Maronsson, T. Maxson, T. Olsen, L. Pastewka, A. Peterson, C. Rostgaard, J. Schiøtz, O. Schütt, M. Strange, K.S. Thygesen, T. Vegge, L. Vilhelmsen, M. Walter, Z. Zeng and K.W. Jacobsen, *Journal of Phys.: Condens. Matter* 2017, **29**, 273002.
6. J.K. Nørskov, J. Rossmeisl, A. Logadottir, L. Lindqvist, J. R. Kitchin, T. Bligaard and H. Jónsson, *J. Phys. Chem. B* 2004, **108**, 17886-17892.
7. *CRC Handbook of Chemistry and Physics, 93rd ed.*; CRC Press: Boca Raton, FL, 2011-2012.
8. L.C. Grabow, B. Hvolbæk, H. Falsig and J.K. Nørskov, *Top. Catal.* 2012, **55**, 336-344.
9. L. Fumagalli, A. Esfandiari, R. Fabregas, S. Hu, P. Ares, A. Janardanan, Q. Yang, B. Radha, T. Taniguchi, K. Watanabe, G. Gomila, K. S. Novoselov and A. K. Geim, *Science* 2018, **360**, 1339-1342.
10. S.R. Kelly, C. Kirk, K. Chan and J.K. Nørskov, *J. Phys. Chem. C* 2020, **124**, 14581-14591.
11. D. Zhang, Z. Wang, F. Liu, P. Yi, L. Peng, Y. Chen and H. Li, *J. Am. Chem. Soc.* 2024, **146**, 3210-3219.
12. K. Mathew, V.S.C. Kolluru, S. Mula, S.N. Steinmann and R.G. Hennig, *J. Chem. Phys.* 2019, **151**, 234101.
13. K. Mathew, R. Sundararaman, K. Letchworth-Weaver, T.A. Arias and R.G. Hennig, *J. Chem. Phys.* 2014, **140**, 084106.
14. S. Trasatti, *Electrochim. Acta* 1991, **36**, 1659-1667.
15. H.A. Hansen, V. Viswanathan and J.K. Nørskov, *J. Phys. Chem. C* 2014, **118**, 6706-6718.
16. A. J. Medford, C. Shi, M. J. Hoffmann, A. C. Lausche, S. R. Fitzgibbon, T. Bligaard and J. K. Nørskov, *Catal. Lett.* 2015, **145**, 794-807.
17. C.F. Dickens, C. Kirk and J.K. Nørskov, *J. Phys. Chem. C* 2019, **123**, 18960-18977.
18. V. Viswanathan, H.A. Hansen, J. Rossmeisl and J.K. Nørskov, *J. Phys. Chem. Lett.* 2012, **3**, 2948-2951.
19. J. Pei, H. Shang, J. Mao, Z. Chen, X. Zhang, D. Zhou, Y. Wang, F. Zhang, W. Zhu, T. Wang, W. Chen and Z. Zhuang, *Nat. Commun.* 2024, **15**, 416.
20. P. Li, Y. Jiao, Y. Ruan, H. Fei, Y. Men, C. Guo, Y. Wu and S. Chen, *Nat. Commun.* 2023, **14**, 6936.
21. Q. Wang, S. Tang, Z. Wang, J. Wu, Y. Bai, Y. Xiong, P. Yang, Y. Wang, Y. Tan, W. Liu, X. Xiong and Y. Lei, *Adv. Funct. Mater.* 2023, **33**, 2307390.
22. Y. Li, X. Liu, L. Zheng, J. Shang, X. Wan, R. Hu, X. Guo, S. Hong and J. Shui, *J. Mater. Chem. A* 2019, **7**, 26147-26153.
23. Y. Ha, B. Fei, X. Yan, H. Xu, Z. Chen, L. Shi, M. Fu, W. Xu and R. Wu, *Adv. Energy Mater.* 2020, **10**, 2002592.
24. Z. Lu, B. Wang, Y. Hu, W. Liu, Y. Zhao, R. Yang, Z. Li, J. Luo, B. Chi, Z. Jiang, M. Li, S. Mu, S. Liao, J. Zhang and X. Sun, *Angew. Chem. Int. Ed.* 2019, **9**, 2622-2626.
25. H. Li, Y. Wen, M. Jiang, Y. Yao, H. Zhou, Z. Huang, J. Li, S. Jiao, Y. Kuang and S. Luo, *Adv. Energy Mater.* 2021, **31**, 2011289.
26. Y. Wang, Y.-J. Tang and K. Zhou, *J. Am. Chem. Soc.* 2019, **36**, 14115-14119.
27. J. Li, H. Li, W. Xie, S. Li, Y. Song, K. Fan, J. Y. Lee and M. Shao, *Small Methods* 2022, **6**, 2101324.
28. J. Chen, H. Li, C. Fan, Q. Meng, Y. Tang, X. Qiu, G. Fu and T. Ma, *Adv. Mater.* 2020, **32**, 2003134.
29. S.-N. Zhao, J.-K. Li, R. Wang, J. Cai and S.-Q. Zang, *Adv. Mater.* 2021, **34**, 2107291.

30. C.-X. Zhao, J.-N. Liu, J. Wang, C. Wang, X. Guo, X.-Y. Li, X. Chen, L. Song, B.-Q. Li and Q. Zhang, *Sci. Adv.* 2022, **8**, eabn5091.
31. Z. Pei, H. Zhang, Y. Guo, D. Luan, X. Gu, X. Wen and D. Lou, *Adv. Mater.* **2023**, *36*, 2306047.
32. Y. Ma, J. Li, X. Liao, W. Luo, W. Huang, J. Meng, Q. Chen, S. Xi, R. Yu, Y. Zhao, L. Zhou and L. Mai. *Adv. Funct. Mater.* 2020, **30**, 2005000.
33. S. Zhang, W. Yang, Y. Liang, X. Yang, M. Cao and R. Cao, *Appl. Catal. B* 2021, **285**, 119780.
34. M. Tong, F. Sun, Y. Xie, Y. Wang, Y. Yang, C. Tian, L. Wang and H. Fu, *Angew. Chem. Int. Ed.* 2021, **60**, 14005-14012.
35. Y. Li, R. Cao, L. Li, X. Tang, T. Chu, B. Huang, K. Yuan and Y. Chen, *Small* 2020, **16**, 2070053.
36. X. Han, X. Ling, D. Yu, D. Xie, L. Li, S. Peng, C. Zhong, N. Zhao, Y. Deng and W. Hu, *Adv. Mater.* 2019, **31**, 1905622.
37. Y. Ma, Y. Yu, J. Wang, J. Lipton, H.N. Tan, L. Zheng, T. Yang, Z. Liu, X.J. Loh, S.J. Pennycook, L. Shen, Z. Kou, A.D. Taylor and J. Wang, *Adv. Sci.* 2022, **9**, 2105192.
38. X. Lei, Q. Tang, Y. Zheng, P. Kidkhunthod, X. Zhou, B. Ji and Y. Tang, *Nat. Sustain.* 2023, **6**, 816-826.
39. Y. Wang, Q. Li, L.-C. Zhang, Y. Wu, H. Chen, T. Li, M. Xu and S.-J. Bao, *J. Mater. Chem. A* 2021, **9**, 7137-7142.
40. J. Ji, L. Wu, S. Zhou, T. Qiu, Z. Li, L. Wang, L. Zhang, L. Ma, M. Ling, S. Zhou and Liang, C. *Small Methods* 2022, **6**, 2101511.
41. M. Shen, J. Liu, C. Duan, C. Xiong, W. Zhao, L. Dai, Q. Wang, H. Yang and Y. Ni, *Energy Storage Mater.* 2023, **59**, 102790.
42. Z. Wang, C. Zhu, H. Tan, J. Liu, L. Xu, Y. Zhang, Y. Liu, X. Zou, Z. Liu and X. Lu, *Adv. Funct. Mater.* 2021, **31**, 2104735.
43. G. Wang, J. Chang, S. Koul, A. Kushima and Y. Yang, *J. Am. Chem. Soc.* 2021, **143**, 11595-11601.
44. F. F. Shahbazi, M. S. Rahmanifar, A. Noori, M. F. El-Kady, N. Hassani, M. Neek-Amal, R. B. Kaner and M. F. Mousavi, *J. Am. Chem. Soc.* 2022, **144**, 3411-3428.
45. M. Liu, X. Wang, S. Cao, X. Lu, W. Li, N. Li and X.-H. Bu, *Adv. Mater.* 2024, **36**, 2309231.
46. Y. Wang, J. Wu, S. Tang, J. Yang, C. Ye, J. Chen, Y. Lei and D. Wang, *Angew. Chem. Int. Ed.* 2023, **62**, e202219191.
47. Y.-X. Zhao, J.-H. Wen, P. Li, P.-F. Zhang, S.-N. Wang, D.-C. Li, J.-M. Dou, Y.-W. Li, H.-Y. Ma and L. Xu, *Angew. Chem. Int. Ed.* 2023, **62**, e202216950.
48. T. Liu, S. Zhao, Y. Wang, J. Yu, Y. Dai, J. Wang, X. Sun, K. Liu and M. Ni, *Small* 2021, **18**, 2105887.
49. H. Meng, B. Wu, D. Zhang, X. Zhu, S. Luo, Y. You, K. Chen, J. Long, J. Zhu, L. Liu, S. Xi, T. Petit, D. Wang, X.-M. Zhang, Z. J. Xu and L. Mai, *Energy Environ. Sci.* 2024, **17**, 704-716.
50. L. Li, N. Li, J. Xia, S. Zhou, X. Qian, F. Yin, G. He and H. Chen, *J. Mater. Chem. A* 2023, **11**, 2291-2301.
51. K. Yuan, D. Lützenkirchen-Hecht, L. Li, L. Shuai, Y. Li, R. Cao, M. Qiu, X. Zhuang, Michael. K. H. Leung, Y. Chen and U. Scherf, *J. Am. Chem. Soc.* 2020, **142**, 2404-2412.
52. S. Zhu, L. Ding, X. Zhang, K. Wang, X. Wang, F. Yang and G. Han, *Angew. Chem. Int. Ed.* 2023, **62**, e2023095.
53. Y. Zhou, Y. Liu, Z. Wang, C. Li, Z. Wang, S. Zhang and C. Deng, *Energy Storage Mater.* 2023, **59**, 102772.
54. H. Jiang, J. Xia, L. Jiao, X. Meng, P. Lee, C.-S. Wang and W. Zhang, *Appl. Catal. B* 2022, **310**, 121352.
55. J.-N. Liu, C.-X. Zhao, J. Wang, X.-Q. Fang, C.-X. Bi, B.-Q. Li and Q. Zhang, *Joule* 2024, **8**, 1804-1819.
56. H. Chang, X. Liu, S. Zhao, Z. Liu, R. Lv, Q. Zhang and T.-F. Yi, *Adv. Funct. Mater.* 2023, **16**, 2313491.
57. X. Shu, S. Chen and J. Zhang, *Adv. Energy Mater.* 2022, **13**, 2202871.
58. Q. Zhou, W. Xue, X. Cui, P. Wang, S. Zuo, F. Mo, C. Li, G. Liu, S. Ouyang, S. Zhan, J. Chen and C. Wang, *Proc. Natl Acad. Sci. USA* 2024, **121**, e2404013121.

59. M. Dan, X. Zhang, Y. Yang, J. Yang, F. Wu, S. Zhao and Z.-Q. Liu, *Proc. Natl Acad. Sci. USA* 2024, **121**, e2318174121.
60. X. Hu, X. Chen, X. Li and C. Xu, *Adv. Funct. Mater.* 2024, **34**, 2316699.
61. J. Zhong, Z. Liang, N. Liu, Y. Xiang, B. Yan, F. Zhu, X. Xie, X. Gui, L. Gan, H. B. Yang, D. Yu, Z. Zeng and G. Yang, *ACS Nano* 2024, **18**, 5258-5269.
62. C. Lv, B. Li, Y. Ren, G. Zhang, Z. Lu, L. Li, X. Zhang, X. Yang and X. Yu, *Chem. Eng. J.* 2024, **495**, 153670.
63. L. Yang, C. Du, J. Tian, X. Yao, Q. Zhang, X. Ma, Y. Zhu, M. Zou, C. Cao, *Appl. Catal. B* 2024, **355**, 124190.